



Stability of cylindrical, multicomponent vesicles

Anirudh Venkatesh¹, Aman Bhargava¹ and Vivek Narsimhan^{1,†}

¹Davidson School of Chemical Engineering, Purdue University, West Lafayette, IN 47907, USA

(Received 26 February 2024; revised 6 November 2024; accepted 10 November 2024)

Vesicles are important surrogate structures made up of multiple phospholipids and cholesterol distributed in the form of a lipid bilayer. Tubular vesicles can undergo pearling – i.e. formation of beads on the liquid thread akin to the Rayleigh–Plateau instability. Previous studies have inspected the effects of surface tension on the pearling instabilities of single-component vesicles. In this study, we perform a linear stability analysis on a multicomponent cylindrical vesicle. We solve the Stokes equations along with the Cahn–Hilliard equation to develop the linearized dynamic equations governing the vesicle shape and surface concentration fields. This helps us to show that multicomponent vesicles can undergo pearling, buckling and wrinkling even in the absence of surface tension, which is a significantly different result from studies on single-component vesicles. This behaviour arises due to the competition between the free energies of phase separation, line tension and bending for this multi-phospholipid system. We determine the conditions under which axisymmetric and non-axisymmetric modes are dominant, and supplement our results with an energy analysis that shows the sources for these instabilities. Lastly, we delve into a weakly nonlinear analysis where we solve the nonlinear Cahn–Hilliard equation in the weak deformation limit to understand how mode-mixing alters the late time dynamics of coarsening. We show that in many situations, the trends from our simulations qualitatively match recent experiments (Yanagisawa *et al.*, *Phys. Rev. E*, vol. 82, 2010, p. 051928).

Key words: membranes

1. Introduction

Vesicles are miniature sacs of fluids surrounded by a thin lipid bilayer, which are often studied to understand the biophysics of cell membranes (Lipowsky & Seifert 1995; Litschel & Schwille 2021). The lipid bilayer demonstrates elasticity that resists changes in

† Email address for correspondence: vnarsim@purdue.edu

area and bending, and these properties make vesicle dynamics different from conventional fluid droplets (Helfrich 1973; Seifert 1997).

Vesicles that contain a single lipid species are known as single-component vesicles. Deflated vesicles of this form demonstrate a wide range of behaviours such as tank treading, tumbling and trembling under shear flow (Vlahovska & Gracia 2007; Deschamps *et al.* 2009; Abreu *et al.* 2014), and stretching instabilities under extensional flow (Boedec, Jaeger & Leonetti 2014; Narsimhan 2014; Narsimhan, Spann & Shaqfeh 2015). When a tubular vesicle is subject to an external force or perturbation, it may undergo a Rayleigh–Plateau-like instability known as ‘pearling’ under tension (Bar-Ziv & Moses 1994; Granek & Olami 1995; Goldstein *et al.* 1996; Gurin, Lebedev & Muratov 1996; Bar-Ziv, Moses & Nelson 1998; Powers 2010; Pullarkat *et al.* 2010; Agrawal & Steigmann 2011; Boedec *et al.* 2014) and buckling/wrinkling instabilities under compression (Narsimhan *et al.* 2015). The pearling phenomenon has been observed for liquid drops (Tomotika 1935), jets (Suryo, Doshi & Basaran 2007) and effective viscoelastic media (Rahimi, DeSimone & Arroyo 2011). Recently, linear stability analyses have been performed on single-component, tubular vesicles to quantify the onset of pearling, buckling and wrinkling modes, including the effects of membrane’s bending rigidity, surface viscosity and applied tension (Narsimhan *et al.* 2015).

In most biological, pharmaceutical and industrial applications, lipid bilayers contain multiple phospholipids and cholesterol mixtures. These mixtures form phase-separated domains – i.e. lipid rafts – that are vitally important in signal transduction and protein transport across the cell membrane in biology (Simons & Ikonen 1997). This behaviour arises due to the repulsive interactions between saturated and unsaturated lipids on the interface, leading to a liquid-ordered (cholesterol rich) phase and a liquid-disordered (cholesterol poor) phase on the interface (Shimshick & McConnell 1973; Veatch & Keller 2003; Elson *et al.* 2010). Under these conditions, phase separation on the vesicle surface causes inhomogeneities in material properties like the bending stiffness (Claessens *et al.* 2007). These inhomogeneous properties make for interesting physics under flow and is important in understanding a multitude of physical processes (Baumgart, Hess & Webb 2003; Barthès-Biesel 2016; Gera, Salac & Spagnolie 2022; Bachini *et al.* 2023a; Yu & Košmrlj 2023). For example, recent experiments have shown that phase-separated vesicles can give rise to pearling and buckling instabilities (Yanagisawa, Imai & Taniguchi 2010).

In this paper, we perform a linear stability analysis of a cylindrical thread with multiple lipids on it, and determine the conditions under which it is unstable under tension or compression. We will discuss how these results differ from the classical results for a single-component vesicular thread and perform a qualitative comparison with recent experimental results on multicomponent threads. Section 2 lays out the mathematical formulation of the problem and outlines the characteristic time scales and dimensionless quantities governing the system. This is followed by the linear stability analysis and final reduced equations in § 3. We refresh the memory of the reader by providing results for single-component vesicles in § 4. In § 5, we first provide a general set of observations pertaining to multicomponent vesicles. We then describe the conditions under which one observes axisymmetric versus non-axisymmetric instabilities, and quantify growth rates and dominant wavenumbers. Interestingly, we find that under certain situations, one can observe multimodal instabilities since the growth rates for the axisymmetric and non-axisymmetric modes are comparable. We also discuss the role of surface viscosity and Péclet number (comparing coarsening and bending time scales) on the growth rates of the instability, and provide an energy analysis to describe which energetic contributions drive the instability. Lastly, in § 6, we perform a weakly nonlinear analysis where we solve the fully nonlinear Cahn–Hilliard equations in the weak deformation limit. This

analysis is performed to understand the limits of the linear stability analysis and to improve our understanding of the long-time dynamics where mode mixing could come into play. We provide qualitative comparisons to previous experimental studies (Yanagisawa *et al.* 2010). Conclusions are in § 7.

2. Mathematical formulation

Figure 1 shows an initially cylindrical lipid membrane with Newtonian fluids inside and outside with viscosities $\lambda\mu$ and μ , respectively. The membrane contains multiple phospholipids that are initially well mixed, but can potentially phase separate into liquid-ordered (L_o) and liquid-disordered domains (L_d). The membrane is incompressible and characterized by an isotropic surface tension σ_0 , a spatially varying bending modulus κ_c and a line tension between the domains (characterized by parameter γ described later in this section). We will perform a linear stability analysis by perturbing the membrane shape and lipid concentration, and determine how the shape and phase behaviour evolve over time. In § 6, we will perform a weakly nonlinear analysis.

2.1. Membrane energy

The energy of the lipid membrane is governed by three factors: bending, phase energy and surface tension. The bending energy is given by the classic Canham–Helfrich model (Helfrich 1973):

$$W_{bend} = \int \frac{1}{2}\kappa_c H^2 dS + \int \frac{1}{2}\kappa_g K dS. \quad (2.1)$$

In the above equation, $H = \frac{1}{2}\nabla_s \cdot \mathbf{n}$ is the mean curvature of the membrane and K is the Gaussian curvature (see § A.1), where \mathbf{n} is the outward-pointing normal vector and $\nabla_s = (\mathbf{I} - \mathbf{nn}) \cdot \nabla$ is the surface gradient operator. The bending modulus κ_c depends on the lipid distribution on the membrane. We represent it as $\kappa_c = ((\kappa_{lo} + \kappa_{ld})/2) + ((\kappa_{lo} - \kappa_{ld})/2)q$, where κ_{lo} and κ_{ld} are bending moduli of the L_o and L_d phases, and q is an order parameter that represents the phase behaviour of the system ($q = -1$ corresponds to pure L_d phase, while $q = +1$ corresponds to pure L_o phase). Going forward, we will denote $k_0 = ((\kappa_{lo} + \kappa_{ld})/2)$ as the average bending rigidity and $k_1 = ((\kappa_{lo} - \kappa_{ld})/2)$ as half the bending difference. Thus, $\kappa_c = k_0 + k_1q$.

In our paper, we will neglect the effect of Gaussian bending rigidity κ_g . While some studies show that the membrane tractions and chemical potentials are altered by a linear variation κ_g with respect to the order parameter q (Amazon, Goh & Feigenson 2013; Barrett, Garcke & Nürnberg 2017), this effect plays no role in the linear stability analysis as its effect on these quantities is $O(\epsilon^2)$, where ϵ is the magnitude of the perturbation. A future study can consider its role in the nonlinear coarsening dynamics.

The order parameter q is determined by the thermodynamics of mixing between the membrane’s phospholipids. There are many thermodynamic models available in the literature depending on the specific type of lipids involved and the level of accuracy required (Almeida 2009). However, the simplest model that qualitatively captures the physics of phase separation is the Landau–Ginzberg equation (Safran 2018). Physically, when one marches along the coordinate that represents a tie line in a phase diagram, the free energy will have two local minima with a barrier in-between if phase

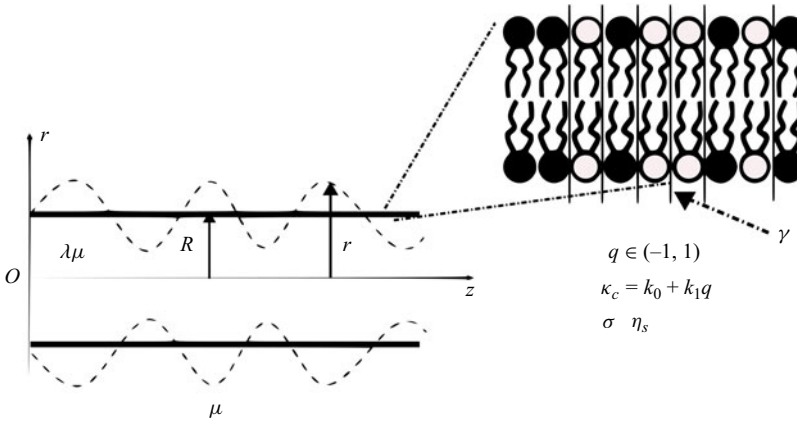


Figure 1. Problem set-up. We examine the stability of a cylindrical vesicle with Newtonian fluid inside and outside with viscosities $\lambda\mu$ and μ , respectively. The membrane has multiple lipids and is characterized by an order parameter q representing different phase-separated domains, a bending modulus κ_c depending on q , a line tension parameter γ , surface viscosity η_s and surface tension σ .

separation occurs. The simplest shape that represents this behaviour is a quartic polynomial, and hence one can write the free energy as

$$W_{phase} = \int \left(\frac{a}{2}|q|^2 + \frac{b}{4}|q|^4 + \frac{\gamma^2}{2}|\nabla_s q|^2 \right) dS, \quad (2.2)$$

where q is the order parameter (i.e. coordinate along the tie line for the two phases). The first two terms in the equation represent a quartic free energy with two minima (i.e. two phases) when $a < 0$, and one minima (i.e. one phase) when $a > 0$. The last term is the free energy penalty for creating phases that is related to line tension (ξ^{line}) and the interface width (ε^{width}):

$$\xi^{line} = \frac{2\sqrt{2}}{3b}a^{3/2}\gamma, \quad (2.3)$$

$$\varepsilon^{width} = \sqrt{\frac{2\gamma^2}{a}}. \quad (2.4)$$

The Landau–Ginzberg equation has been used to qualitatively model bilayer membranes (Gera & Salac 2017). Specifically, the symmetric form of the Landau–Ginzberg equation listed above gives reasonable estimates for the L_o/L_d phase-coexistence for the case of a 1 : 1 : 1 ratio of DOPC : DPPC : cholesterol membranes – see the appendix of Camley & Brown (2014) for the estimated dependence of a , b and γ for a specific experimental system ($R \sim O(nm)$).

The last contribution to the free energy arises from surface tension,

$$W_\sigma = \int \sigma dS. \quad (2.5)$$

Since the number of lipids per unit area is conserved, the membrane surface is incompressible. Thus, σ is a Lagrange multiplier used to ensure this constraint. The surface tension is determined up to an isotropic component σ_0 , which is specified beforehand. When $\sigma_0 > 0$, the membrane is initially under tension, while when $\sigma_0 < 0$, the membrane is initially under compression.

2.2. Dynamical equations

We solve the fluid flow inside and outside the membrane in the limit of vanishing Reynolds number. The Stokes equations are

$$\mu^{in} \nabla^2 \mathbf{u}^{in} = \nabla p^{in}; \quad \nabla \cdot \mathbf{u}^{in} = 0, \tag{2.6a}$$

$$\mu^{out} \nabla^2 \mathbf{u}^{out} = \nabla p^{out}; \quad \nabla \cdot \mathbf{u}^{out} = 0, \tag{2.6b}$$

where (\mathbf{u}, p) are the velocity and pressure fields, and $\mu^{in/out}$ are the viscosities inside and outside the vesicle ($\mu^{in} = \lambda\mu, \mu^{out} = \mu$). These equations satisfy continuous velocity across the interface:

$$[[\mathbf{u}]] = 0 \quad \mathbf{x} \in S, \tag{2.7}$$

where $[[\dots]]$ represents the jump across the interface (outer minus inner). The membrane is surface incompressible:

$$\nabla_s \cdot \mathbf{u} = 0 \quad \mathbf{x} \in S. \tag{2.8}$$

Lastly, the hydrodynamic tractions on the interface are balanced by the membrane tractions,

$$[[\mathbf{n} \cdot \boldsymbol{\tau}]] = \frac{\delta W}{\delta \mathbf{x}} + \mathbf{f}^{s-v} \quad \mathbf{x} \in S. \tag{2.9}$$

In the above equation, $\boldsymbol{\tau}^{in/out} = -p^{in/out} \mathbf{I} + \mu^{in/out} (\nabla \mathbf{u}^{in/out} + (\nabla \mathbf{u}^{in/out})^T)$ is the viscous stress tensor. The term \mathbf{f}^{s-v} represents the tractions arising from the surface viscosity effects in the bilayer. This term is representative of the frictional forces existing within the bilayer due to phospholipids. The other term on the right side is the first variation of the membrane energy with respect to position. This term can be broken into different contributions $\delta W / \delta \mathbf{x} = \mathbf{f}^{phase} + \mathbf{f}^{bend} + \mathbf{f}^\sigma$, with expressions for each of them listed below:

$$\mathbf{f}^{phase} = \frac{\delta W_{phase}}{\delta \mathbf{x}} = -\gamma^2 (\nabla_s^2 q) \nabla_s q - \nabla_s g + 2H \left(\frac{1}{2} \gamma^2 |\nabla_s q|^2 + g \right) \mathbf{n}, \tag{2.10a}$$

$$\mathbf{f}^{bend} = \frac{\delta W_{bend}}{\delta \mathbf{x}} = -\mathbf{n} \nabla_s^2 (2H\kappa_c) + \kappa_c (4HK - 4H^3) \mathbf{n} - 2H^2 \nabla_s \kappa_c, \tag{2.10b}$$

$$\mathbf{f}^\sigma = \frac{\delta W_\sigma}{\delta \mathbf{x}} = 2H\sigma \mathbf{n} - \nabla_s \sigma, \tag{2.10c}$$

$$\mathbf{f}^{s-v} = \nabla_s \cdot [\eta_s (\mathbf{P} (\nabla_s \cdot \mathbf{u}) - \mathbf{P} \cdot (\nabla_s \mathbf{u} + \nabla_s \mathbf{u}^T) \cdot \mathbf{P})]. \tag{2.10d}$$

The reader is directed to the following publications for details on how these equations are derived (Napoli & Vergori 2010; Gera 2017; Sahu, Sauer & Mandadapu 2017). In the above equations, $g = (a/2)q^2 + (b/4)q^4$ is the quartic free energy and $\mathbf{P} \equiv \mathbf{I} - \mathbf{nn}$. Additionally, $K = \det(\mathbf{L}) = C_1 C_2$ is the Gaussian curvature of the interface, where $\mathbf{L} = \nabla_s \mathbf{n}$ is the surface curvature tensor and C_1, C_2 denote the principal curvatures. The surface tension σ is a Lagrange multiplier (up to a specified isotropic constant), which one determines from the surface incompressibility constraint equation (2.8) listed above.

Along with the above flow equations, we also solve a convection-diffusion equation on the vesicle interface for the order parameter q . This equation takes the form of a Cahn–Hilliard equation, the details of which can be found from Gera (2017),

$$\frac{\partial q}{\partial t} + \mathbf{u} \cdot \nabla_s q = \frac{\nu}{\zeta_0} \nabla_s^2 (\zeta) \quad \mathbf{x} \in S. \quad (2.11)$$

In the above equation, ν is the characteristic mobility of the phospholipids and ζ is the surface chemical potential with units of energy per unit area. This chemical potential is the first variation of the membrane energy with respect to the order parameter, while ζ_0 is a reference value provided by Gera (2017),

$$\zeta = \frac{\delta W}{\delta q} = aq + bq^3 - \gamma^2 \nabla_s^2 q + \frac{k_1}{2} (2H)^2. \quad (2.12)$$

Lastly, the interface satisfies a kinematic boundary condition. If the vesicle’s shape is characterized by the level set $r = f(z, \phi, t)$, this condition is

$$\frac{D}{Dt} (r - f(z, \phi, t)) = 0, \quad \frac{D}{Dt} = \frac{\partial}{\partial t} + \mathbf{u} \cdot \nabla. \quad (2.13a,b)$$

2.3. Physical parameters and dimensionless numbers

Unless otherwise noted, all remaining quantities in the manuscript will be in dimensionless form. We non-dimensionalize all lengths by cylinder radius R , all times by the bending time scale $t_b = \mu R^3/k_0$ and all velocities by $U_b = R/t_b = k_0/(\mu R^2)$. All pressures and stresses are scaled by $\mu U_b/R = k_0/R^3$, and the surface tension is scaled by k_0/R^2 . Energies are scaled by k_0 and chemical potential is scaled by k_0/R^2 . Table 1 lists the set of physical parameters for this problem and their typical experimental values, while table 2 lists the dimensionless numbers for this problem. These dimensionless groups are related to the effects of line tension between the phospholipids, the relative magnitudes of bending stiffness of phospholipids and size of the vesicle – depicting an interplay between bending, coarsening and flow. The most important ones in particular are the viscosity ratio λ between the inner and outer fluid, the dimensionless surface tension $\Gamma = \sigma_o R^2/k_0$, the dimensionless bending stiffness difference between the two phases $\beta = k_1/k_0 = (\kappa_{lo} - \kappa_{ld})/(\kappa_{lo} + \kappa_{ld})$, the Cahn number $Cn = \gamma/(R\sqrt{\zeta_0})$ (i.e. ratio of line tension energy to the energy scale of phase separation), the surface Péclet number $Pe = k_0/(\nu\mu R)$ (i.e. ratio of coarsening time to bending time from diffusion) and the line tension parameter $\alpha = k_0/\gamma^2$ (ratio between bending and line tension energies). Another important variable to consider is the membrane viscosity η_s (Faizi, Dimova & Vlahovska 2022). This parameter represents the frictional forces that exist between the phospholipids. On non-dimensionalizing this variable, we get the Boussinesq number $Bq = \eta_s/(\mu R)$. Some studies have reported simple correlations to relate the surface viscosity to the phospholipid phase concentration, which could be traced to the order parameter q (Sakuma *et al.* 2020). We treat the surface viscosity to vary linearly with the order parameter $\eta_s = \eta_1 + \eta_2 q$, along similar lines as the bending modulus variation where $\eta_1 = (\eta_{so} + \eta_{sd})/2$ is the average surface viscosity of the two phases and $\eta_2 = (\eta_{so} - \eta_{sd})/2$ is half the difference of surface viscosities between the two phases. Lastly, we note that for $\zeta_0 = |a|$, as is the case for most studies, the Cahn number has the alternative interpretation as the ratio of interface width to vesicle radius: $Cn = \varepsilon^{width}/(\sqrt{2}R)$. See § A.2 for details.

Physical governing parameters			
Variable	Name	Order of magnitude	Reference
L	Length of cylindrical vesicle	$\sim 30 \mu\text{m}$	Kantsler, Segre & Steinberg (2008)
R	Radius of cylindrical vesicle	$\sim 5 \mu\text{m}$	Kantsler <i>et al.</i> (2008)
k_0	Bending stiffness sum between phospholipid 1 and 2	$O(10^{-19} - 10^{-18}) \text{ J}$	Amazon <i>et al.</i> (2013)
k_1	Bending stiffness difference between phospholipid 1 and 2	$O(10^{-19}) \text{ J}$	Amazon <i>et al.</i> (2013)
ν	Mobility of phospholipids	$O(10^{-11}) \text{ m}^2 \text{ s}^{-1}$	Negishi <i>et al.</i> (2008)
γ	Line tension parameter	$O(10^{-9}) \text{ J}^{1/2}$	Luo & Maibaum (2020)
η_s	Surface viscosity of phospholipids	$O(10^{-9} - 10^{-6}) \text{ Pa m s}$	Sakuma <i>et al.</i> (2020)
κ_g	Gaussian bending rigidity	$O(10^{-19} - 10^{-18}) \text{ J}$	Sakuma <i>et al.</i> (2020)
μ	Bulk viscosity	$O(10^{-3}) \text{ Pa s}$	Sakuma <i>et al.</i> (2020)

Table 1. Physical parameter ranges and orders of magnitude.

Variable	Name	Order of magnitude
L/R	Length to radius ratio	~ 5
$\tilde{a} = a/\xi_0$	Dimensionless double well potential term	-1
$\tilde{b} = b/\xi_0$	Dimensionless double well potential term	$O(1)$
$\beta = k_1/k_0$	Ratio of bending stiffnesses	$O(0.1-1)$
$Cn = \gamma/(R\sqrt{\xi_0}) = \varepsilon^{width}/(\sqrt{2}R)$	Cahn number	$O(0.1-1)$
$\alpha = k_0/\gamma^2$	Ratio of bending stiffness to line tension	$O(1)$
λ	Viscosity ratio	$O(1-10)$
$Pe = k_0/(\nu\mu R)$	Péclet number (coarsening time scale/bending time scale)	$O(1)-O(100)$
$\Gamma = \sigma_0 R^2/k_0$	Dimensionless isotropic membrane tension	$O(1-10)$
$Bq = \eta_1/(R\mu)$	Boussinesq number	$O(1-1000)$

Table 2. Dimensionless parameter ranges and orders of magnitude.

3. Linear stability analysis

3.1. Derivation

We consider a vesicle that has its base state equal to that of a cylinder at rest (i.e. $r_0 = 1$, $\mathbf{u}_0^{in} = \mathbf{u}_0^{out} = 0$). The membrane is uniformly mixed as one phase with an equal amount of stiff and soft lipids (i.e. $q_0 = 0$). The membrane tension is uniform with a non-dimensional value $\Gamma = \sigma_0 R^2/k_0$. The base pressure inside and outside the cylinder is given by the Young–Laplace law with bending rigidity, which corresponds to $p_0^{out} = 0$, $p_0^{in} = \Gamma - \frac{1}{2}$.

We perform a linear stability analysis on this base state. We perturb all geometric and physical quantities an infinitesimal amount $\epsilon \ll 1$, as follows:

$$r = 1 + \epsilon r_{kn} \exp(ikz + in\phi), \tag{3.1a}$$

$$\sigma = \Gamma + \epsilon \sigma_{kn} \exp(ikz + in\phi), \tag{3.1b}$$

$$\mathbf{u}^{in/out} = \epsilon \mathbf{u}_{kn}^{in/out} \exp(ikz + in\phi), \tag{3.1c}$$

$$q = \epsilon q_{kn} \exp(ikz + in\phi), \tag{3.1d}$$

$$p^{in} = \Gamma - \frac{1}{2} + \epsilon p_{kn}^{in} \exp(ikz + in\phi), \tag{3.1e}$$

$$p^{out} = \epsilon p_{kn}^{out} \exp(ikz + in\phi). \tag{3.1f}$$

We then solve the Stokes equations and Cahn–Hilliard equations, linearized to $O(\epsilon)$, and determine how the radius r and concentration field q evolve over time. The thread is considered unstable if a perturbation causes the radius and concentration to grow over time. Due to the geometric nature of the problem, all perturbations are decomposed into Fourier modes, where k and n represent axial and azimuthal wavenumbers.

The first step we perform is to linearize the Cahn–Hilliard equation (that is, (2.11) and (2.12)). Doing so yields a differential equation for the order parameter q_{kn} :

$$F_{kn} \dot{q}_{kn} = M_{kn} r_{kn} + V_{kn} q_{kn}. \tag{3.2}$$

In the above equation, the right-hand side is equal to the linearized chemical potential $\delta W / \delta q$, while the left-hand side is a dynamical factor. The coefficients are given by

$$F_{kn} = -\frac{Pe}{Cn^2\alpha} \frac{1}{k^2 + n^2}, \tag{3.3a}$$

$$M_{kn} = \beta(k^2 + n^2 - 1), \tag{3.3b}$$

$$V_{kn} = \frac{1}{Cn^2\alpha} [\tilde{a} + Cn^2(k^2 + n^2)]. \tag{3.3c}$$

To obtain the differential equation for the vesicle shape r_{kn} , we follow a procedure similar the previous publications for single-component vesicles (see Narsimhan 2014; Narsimhan *et al.* 2015). First, we solve the Stokes equations inside and outside the vesicle. We use the cylindrical harmonics solution given by Happel & Brenner (1973):

$$\mathbf{u}_{kn} \exp(ikz + in\phi) = \nabla \psi + \nabla \times (\Omega \hat{\mathbf{z}}) + r \frac{\partial}{\partial r} (\nabla \Pi) + \hat{\mathbf{z}} \frac{\partial \Pi}{\partial z}, \tag{3.4a}$$

$$p_{kn} \exp(ikz + in\phi) = -2\tilde{\eta} \frac{\partial^2 \Pi}{\partial z^2}, \tag{3.4b}$$

where $\tilde{\eta}$ is the non-dimensional viscosity ($\tilde{\eta} = 1$ outside the vesicle and $\tilde{\eta} = \lambda$ inside), and ψ , Ω and Π are scalar harmonic functions:

$$\{\psi, \Omega, \Pi\} = \{A_{kn}, iB_{kn}, C_{kn}\} G_n(kr) \exp(ikz + in\phi). \tag{3.5}$$

In the above equation, the functions $G_n(kr)$ are modified Bessel functions, equal to $I_n(kr)$ inside the vesicle and $(-1)^n K_n(kr)$ outside the vesicle. Writing the velocity and pressure fields in this form yields seven unknowns for each Fourier mode, which we solve through appropriate boundary conditions. The unknowns are the coefficients $\{A_{kn}^{out}, B_{kn}^{out}, C_{kn}^{out}\}$ outside the vesicle, the coefficients $\{A_{kn}^{in}, B_{kn}^{in}, C_{kn}^{in}\}$ inside the vesicle and the non-isotropic surface tension σ_{kn} that arises from membrane incompressibility.

Below is the structure of the linear equations we solve. The structure is given by $\mathbf{W} \cdot \mathbf{y} = \mathbf{b}$, where \mathbf{W} is a matrix, $\mathbf{y} = \{A_{kn}^{out}, B_{kn}^{out}, C_{kn}^{out}, A_{kn}^{in}, B_{kn}^{in}, C_{kn}^{in}, \sigma_{kn}^M\}$ is the vector of unknowns where $\sigma_{kn}^M = \sigma_{kn} + (\beta/2)q_{kn}$ is a modified surface tension, and \mathbf{b} is the right-hand side. We use a modified surface tension for convenience since the linear system

below becomes exactly the same as in previous literature for single-component vesicles (Narsimhan *et al.* 2015):

$$\begin{bmatrix} W_{11} & W_{12} & W_{13} & W_{14} & W_{15} & W_{16} & W_{17} \\ W_{21} & W_{22} & W_{23} & W_{24} & W_{25} & W_{26} & W_{27} \\ W_{31} & W_{32} & W_{33} & W_{34} & W_{35} & W_{36} & W_{37} \\ W_{41} & W_{42} & W_{43} & W_{44} & W_{45} & W_{46} & W_{47} \\ W_{51} & W_{52} & W_{53} & W_{54} & W_{55} & W_{56} & W_{57} \\ W_{61} & W_{62} & W_{63} & W_{64} & W_{65} & W_{66} & W_{67} \\ W_{71} & W_{72} & W_{73} & W_{74} & W_{75} & W_{76} & W_{77} \end{bmatrix} \begin{bmatrix} A_{kn}^{in} \\ B_{kn}^{in} \\ C_{kn}^{in} \\ A_{kn}^{out} \\ B_{kn}^{out} \\ C_{kn}^{out} \\ \sigma_{kn}^M \end{bmatrix} = \begin{bmatrix} b_1 \\ b_2 \\ b_3 \\ b_4 \\ b_5 \\ b_6 \\ b_7 \end{bmatrix}. \quad (3.6)$$

In the above linear system, each row arises from a boundary condition. The entries are summarized below, where I_n and K_n are evaluated at wavenumber k and I'_n, I''_n, K'_n, K''_n are single and double derivatives evaluated at k . The entries below are exactly the same as those found in the prior literature.

- Row 1: continuity of velocity ($[[u_z]] = 0$ at $r = 1$)

$$\left. \begin{aligned} W_{11} = -kI_n; \quad W_{12} = 0; \quad W_{13} = -k^2I'_n - kI_n; \quad W_{14} = (-1)^n kK_n; \\ W_{15} = 0; \quad W_{16} = (-1)^n k^2K'_n + (-1)^n kK_n; \quad W_{17} = 0; \quad b_1 = 0 \end{aligned} \right\}, \quad (3.7)$$

- Row 2: continuity of velocity ($[[u_\phi]] = 0$ at $r = 1$)

$$\left. \begin{aligned} W_{21} = -nI_n; \quad W_{22} = kI'_n; \quad W_{23} = -nkI'_n + nI_n; \quad W_{24} = (-1)^n nK_n \\ W_{25} = (-1)^{n+1} kK'_n; \quad W_{26} = (-1)^n nkK'_n - (-1)^n nK_n; \quad W_{27} = 0; \quad b_2 = 0 \end{aligned} \right\}, \quad (3.8)$$

- Row 3: kinematic boundary condition ($u_r^{in} = dr/dt$ at $r = 1$)

$$\left. \begin{aligned} W_{31} = kI'_n; \quad W_{32} = -nI_n; \quad W_{33} = k^2I''_n; \quad W_{34} = 0 \\ W_{35} = 0; \quad W_{36} = 0; \quad W_{37} = 0; \quad b_3 = \dot{r}_{kn} \end{aligned} \right\}, \quad (3.9)$$

- Row 4: kinematic boundary condition ($u_r^{out} = dr/dt$ at $r = 1$)

$$\left. \begin{aligned} W_{41} = 0; \quad W_{42} = 0; \quad W_{43} = 0; \quad W_{44} = (-1)^n kK'_n \\ W_{45} = (-1)^{n+1} nK_n; \quad W_{46} = (-1)^n k^2K''_n; \quad W_{47} = 0; \quad b_4 = \dot{r}_{kn} \end{aligned} \right\}, \quad (3.10)$$

- Row 5: surface incompressibility ($\nabla_s \cdot \mathbf{u}^{out} = 0$ at $r = 1$)

$$\left. \begin{aligned} W_{51} = W_{52} = W_{53} = 0; \quad W_{54} = (-1)^n (kK'_n - (n^2 + k^2)K_n) \\ W_{55} = (-1)^n (-nK_n + knK'_n); \\ W_{56} = (-1)^n (k^2K''_n - k(n^2 + k^2)K'_n + (n^2 - k^2)K_n); \quad W_{57} = 0; \quad b_5 = 0 \end{aligned} \right\}, \quad (3.11)$$

- Row 6: tangential stress balance ($[[\tau_{zr}]] + \partial\sigma^M/\partial z - \hat{\mathbf{z}} \cdot \mathbf{f}^{s-v} = 0$ at $r = 1$)

$$\left. \begin{aligned} W_{61} &= -2\lambda kI'_n - Bq((2k^2 + n^2)I_n + n^2I_n); & W_{62} &= \lambda nI_n - BqnkI'_n; \\ W_{63} &= -\lambda(2k^2I''_n + 2kI'_n) - Bq((2k^2 + n^2)(kI'_n + I_n) + n(-nI_n + nkI'_n)); \\ W_{64} &= (-1)^n 2kK'_n; & W_{65} &= (-1)^{n+1} nK_n; & W_{66} &= (-1)^n(2k^2K''_n + 2kK'_n); \\ & & W_{67} &= 1; & b_6 &= 0 \end{aligned} \right\}, \quad (3.12)$$

- Row 7: tangential stress balance ($[[\tau_{\phi r}]] + (1/r)(\partial\sigma^M/\partial\phi) - \hat{\boldsymbol{\phi}} \cdot \mathbf{f}^{s-v} = 0$ at $r = 1$)

$$\left. \begin{aligned} W_{71} &= -\lambda(2nkI'_n - 2nI_n) - Bqnk^2I_n + Bqk^2nI_n; \\ W_{72} &= -\lambda(-n^2I_n + kI'_n - k^2I''_n) + Bqk^3I'_n; \\ W_{73} &= -\lambda(2nk^2I''_n - 2nkI'_n + 2nI_n) + Bqnk^2I_n; \\ W_{74} &= (-1)^n(2nkK'_n - 2nK_n); & W_{75} &= (-1)^n(-n^2K_n + kK'_n - k^2K''_n); \\ W_{76} &= (-1)^n(2nk^2K''_n - 2nkK'_n + 2nK_n); & W_{77} &= n; & b_7 &= 0 \end{aligned} \right\}. \quad (3.13)$$

After we solve for the unknowns, we apply the last boundary condition – the normal stress balance – to obtain the final differential equation for the vesicle shape. The linearized normal stress boundary condition ((2.9)) is

$$-[[p_{kn}]] - \sigma^M_{kn} - (\mathbf{f}^{sv} \cdot \mathbf{n})_{kn} = L_{kn}r_{kn} + M_{kn}q_{kn}, \quad (3.14)$$

where the left-hand side comes from the pressure, surface tension and surface viscous tractions obtained from the unknowns solved above, and the right-hand side comes from the linearized membrane traction $\mathbf{f} = \delta W/\delta \mathbf{x}$ (minus the modified surface tension contribution σ^M_{kn}). The expression for M_{kn} is the same as in (3.3b), while L_{kn} is

$$L_{kn} = \Gamma(n^2 + k^2 - 1) + \frac{3}{2} + 2k^2 + (n^2 + k^2)(n^2 + k^2 - \frac{5}{2}). \quad (3.15)$$

The expression for the left-hand side in (3.14) in terms of the solved coefficients is

$$\begin{aligned} -[[p_{kn}]] - \sigma^M_{kn} - (\mathbf{f}^{sv} \cdot \mathbf{n})_{kn} &= 2k^2(\lambda_n C_{kn}^{in} + (-1)^{n+1} K_n C_{kn}^{out}) - \sigma^M_{kn} \\ &\quad - Bq(2k^2 I_n A_{kn}^{in} + C_{kn}^{in}(2k^3 I'_n + 2k^2 I_n)). \end{aligned} \quad (3.16)$$

Since the latter quantities are linear in the rate of interface deformation \dot{r}_{kn} , we can rewrite the above expression ((3.14)) as

$$\Lambda_{kn} \dot{r}_{kn} = L_{kn}r_{kn} + M_{kn}q_{kn}. \quad (3.17)$$

This (3.17) along with the linearized Cahn–Hilliard equation (3.2) are the dynamical equations obtained for the linear stability analysis. In general, there is no analytical solution for the coefficient Λ_{kn} – it must be computed numerically by inverting the system of (3.6). However, for the specific case of axisymmetric modes ($n = 0$), analytical expressions are available; details are provided in the [Appendix](#), § A.3.

3.2. Final structure of equations

The final form of the dynamical equations are

$$\begin{bmatrix} \Lambda_{kn} & 0 \\ 0 & F_{kn} \end{bmatrix} \cdot \frac{d}{dt} \begin{bmatrix} r_{kn} \\ q_{kn} \end{bmatrix} = \begin{bmatrix} L_{kn} & M_{kn} \\ M_{kn} & V_{kn} \end{bmatrix} \cdot \begin{bmatrix} r_{kn} \\ q_{kn} \end{bmatrix}, \tag{3.18}$$

where entries Λ_{kn} , F_{kn} , L_{kn} , M_{kn} and V_{kn} were described in the previous section (see (3.3a)–(3.3c), (3.15) and text below (3.15)). A few comments are made here.

- (i) The left-hand side entries Λ_{kn} and F_{kn} are purely dynamical quantities that depend on the hydrodynamics of the surrounding fluid as well as the diffusion characteristics of the lipids. They are negative definite – i.e. $\Lambda_{kn}, F_{kn} < 0$, so they do not alter the stability of the system, but play a role in the time scale of the instability as well as mode selection. Here, Λ_{kn} depends on the viscosity ratio λ and Boussinesq number Bq , while F_{kn} depends on the quantity $Pe/(\alpha Cn^2)$, which equals the diffusion time divided by the chemical potential relaxation time.
- (ii) The right-hand side entries L_{kn}, M_{kn}, V_{kn} are related to the second variation in the free energy at the base state $r_{kn}, q_{kn} = 0$:

$$\begin{bmatrix} L_{kn} & M_{kn} \\ M_{kn} & V_{kn} \end{bmatrix} \sim \begin{bmatrix} \frac{\partial^2 W}{\partial r_{kn} \partial r_{kn}} & \frac{\partial^2 W}{\partial r_{kn} \partial q_{kn}} \\ \frac{\partial^2 W}{\partial r_{kn} \partial q_{kn}} & \frac{\partial^2 W}{\partial q_{kn} \partial q_{kn}} \end{bmatrix}. \tag{3.19}$$

Thus, the matrices are only related to the elastic and mixing energies of the system, and depend only on quantities related to the bending moduli, surface tension, line tension and quartic energy potential. Since these matrices are related to the local curvature of the free energy landscape, the sign of eigenvalues determine the relative stability of the system. For example, if the energy is concave down, the system is unstable.

3.3. Modal analysis

We will perform an eigenvalue/eigenvector analysis on the ordinary differential equations (ODEs) in (3.18). For each set of wavenumbers (k, n) , we will write the system of equations in the form $\dot{\mathbf{y}} = \mathbf{M} \cdot \mathbf{y}$, where $\mathbf{y} = [r_{kn}, q_{kn}]$, and then obtain the two eigenvalue/eigenvector pairs for the matrix \mathbf{M} . The shape is considered to be unstable if there is at least one eigenpair that has a positive eigenvalue and a non-zero component in the r_{kn} direction. The most dangerous of the two eigenpairs is the one that has the largest eigenvalue.

We denote the growth rate s for a given wavenumber (k, n) as the largest eigenvalue:

$$s = \max \text{eig}(\mathbf{M}). \tag{3.20}$$

We will determine the range of wavenumbers that lead to instability by obtaining the set of (k, n) that lead to a positive growth rate. The most dangerous mode (k_{max}, n_{max}) is determined by finding (k, n) that maximize the growth rate. Unlike the single-component vesicle case where only the axisymmetric $(n = 0)$ modes are unstable under tension, the multicomponent case can have non-axisymmetric modes $(n > 1)$ being unstable; thus, we will examine a wide range of values (n, k) in this paper and comment on the type of instabilities formed.

4. Single-component analysis

In this section, we review prior literature on single-component vesicles and validate our equations against published results.

For single-component lipid threads, the formation of instabilities depends on one control parameter, the non-dimensionalized surface tension $\Gamma = \sigma_0 R^2 / k_0$. Figure 2 shows pictures of what the instabilities look like. For this paper, we will coin $n = 0$ modes pearling, $n = 1$ modes as buckling and $n > 1$ modes as wrinkling.

Figures 3(a) and 3(b) compare the growth rates for the pearling and buckling modes from our theory against published results in the literature for single-component vesicles (Boedec *et al.* 2014; Narsimhan *et al.* 2015). We obtain single-component results by setting $\beta = 0$, i.e. both phases have the same bending rigidities; $Cn = 0$, which corresponds to zero line tension between the phases; and the double-well potential parameter $\tilde{a} = 0$, which ensures that no phase separation occurs. We find the growth rates from our analysis coincide with those published previously.

Figure 4 presents the most unstable growth rates for the three modes $n = 0, 1, 2$ for different values of the isotropic membrane tension Γ . If the vesicle is under tension ($\Gamma > 0$), the vesicle is stable to all perturbations for tension values $0 < \Gamma < 3/2$. When the tension is above a critical value $\Gamma > 3/2$, axisymmetric pearling modes ($n = 0$) are unstable (i.e. $s > 0$) and non-axisymmetric modes $n > 0$ are stable. When the thread is under compression ($\Gamma < 0$), both axisymmetric $n = 0$ and non-axisymmetric $n > 0$ modes can become unstable. The axisymmetric (pearling) mode is unstable for $\Gamma < -(3 + 4\sqrt{2})/2$, the $n = 1$ (buckling) mode is unstable for $\Gamma < -3/2$, and $n > 1$ (wrinkling) modes are unstable for $\Gamma < -(n^2 - 3/2)$ (Boedec *et al.* 2014; Narsimhan *et al.* 2015).

On inspecting the effect of surface viscosity via Bq , we observe that the buckling and pearling modes are suppressed as Bq increases (see figure 5). For $n \geq 2$ modes, the effect of Bq is not seen largely. This is consistent with previous observations (Narsimhan *et al.* 2015) where the authors attributed this to increased viscous dissipation on the surface.

5. Multicomponent analysis

5.1. General observations and choice of parameter space

Unlike the single-component system that showed only pearling beyond a particular membrane tension (Boedec *et al.* 2014; Narsimhan *et al.* 2015), multicomponent vesicles can exhibit richer dynamics. The existence of phase separation, line tension and bending rigidity inhomogeneities can give rise to a combination of pearling, buckling or wrinkling modes at zero or positive membrane tension. We visualize the shape of some of these modes in figure 6. The blue colour indicates the cholesterol-rich ordered L_o phase whereas the yellow phase indicates the cholesterol-less disordered L_d phase.

In the following subsections, we will explore these instabilities in greater detail. We will choose the following parameters in our simulations. We will examine equiviscous vesicles ($\lambda = 1$) as experiments typically inspect this value (Yanagisawa *et al.* 2010). Unless otherwise noted, we will choose a bending difference parameter $\beta = (\kappa_{lo} - \kappa_{ld}) / (\kappa_{lo} + \kappa_{ld}) = 0.5$, since we find that β in the range listed in table 2 does not qualitatively alter results. We will also choose the Péclet number $1 \leq Pe \leq 100$ consistent with experimental studies (Negishi *et al.* 2008; Luo & Maibaum 2020).

The structure of the remaining sections are as follows. Section 5.2 characterizes which modes are the most dominant and provides a discussion when multimodal instabilities can be present. Section 5.3 quantifies the most unstable wavenumbers. Section 5.4 discusses

Stability of cylindrical, multicomponent vesicles

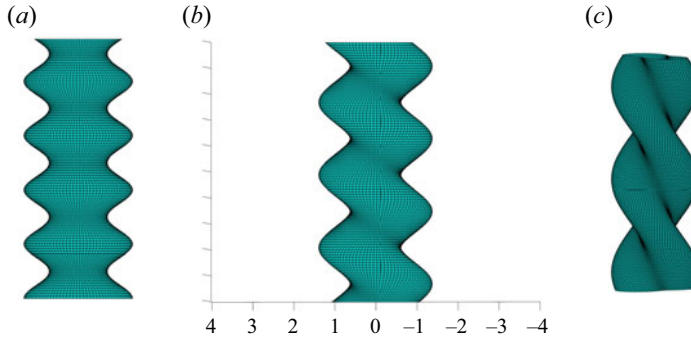


Figure 2. Snapshots of (a) pearling ($n = 0$), (b) buckling ($n = 1$) and (c) wrinkling ($n = 2$) modes for single-component vesicles.

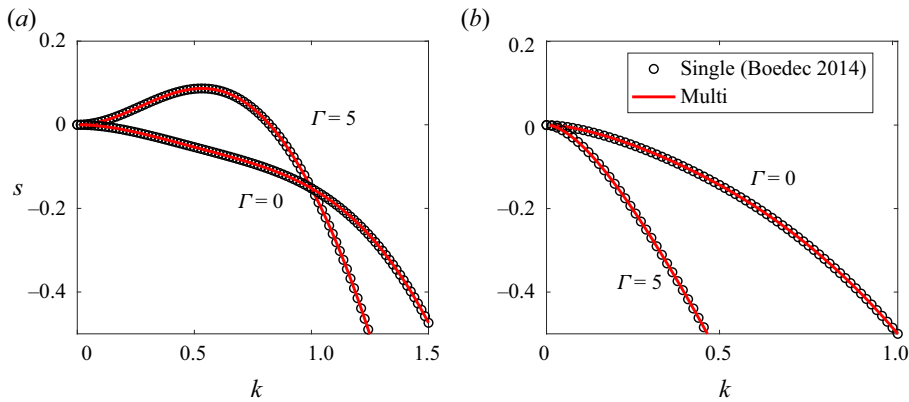


Figure 3. Growth rate versus wavenumber for an equiviscous ($\lambda = 1$), single-component vesicle with no surface viscosity ($Bq = 0$) at $\Gamma = 0$ and $\Gamma = 5$ for (a) pearling mode ($n = 0$) and (b) buckling mode ($n = 1$). Results are validated against published results (Boedec *et al.* 2014).

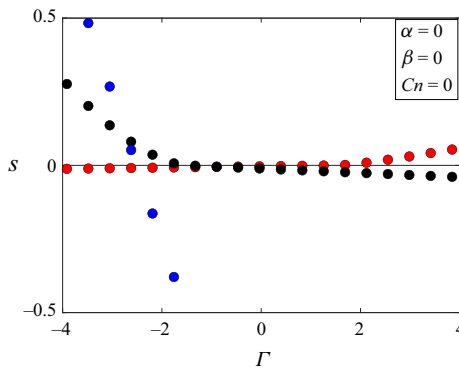


Figure 4. Most unstable growth rates with respect to the isotropic membrane tension Γ for single-component vesicles. The red circles represent $n = 0$ pearling modes, black circles represent $n = 1$ buckling modes and blue circles represent $n = 2$ wrinkling modes. In the plot, $\lambda = 1$, $Bq = 0$.

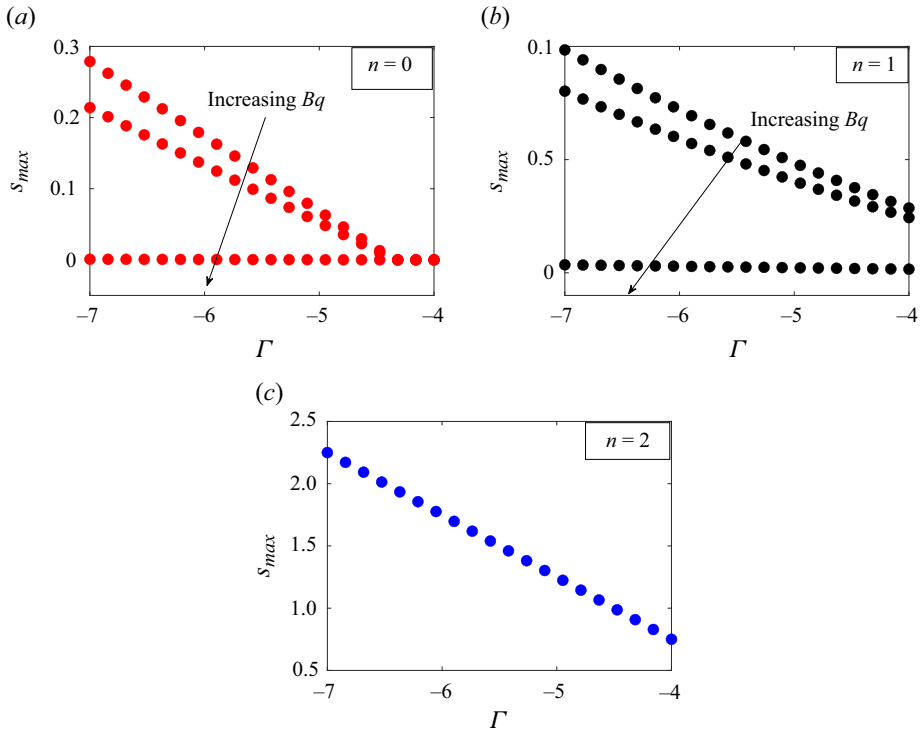


Figure 5. Most unstable growth rates with respect to the isotropic membrane tension Γ for single component vesicles for different values of $Bq = 0.1, 1, 100$. In this plot, $\lambda = 1$. (a) $n = 0$, (b) $n = 1$ and (c) $n = 2$.

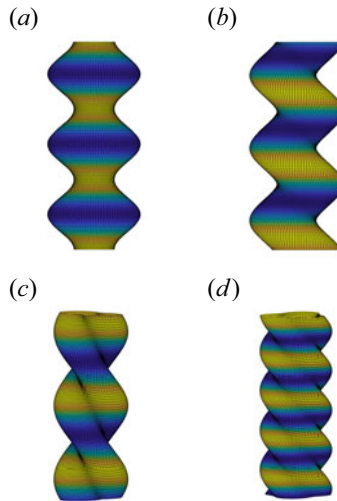


Figure 6. Different unstable modes for multicomponent vesicle: (a) pearling ($n = 0$); (b) buckling ($n = 1$); (c) wrinkling ($n = 2$) and (d) wrinkling ($n = 3$).

the role of Péclet number on the instability, while § 5.5 discusses the role of surface viscosity and provides an analytic expression for when instability occurs. Section 5.6 performs an energy analysis to understand the mechanism of these instabilities. Lastly, we make a side note for the special case of $Pe \ll 1$, where analytical solutions to the eigenvalues and eigenvectors are available. While we believe this case is not physically relevant (see table 2), § A.4 provides details of this analysis for those who are interested.

5.2. Which modes are most dominant?

Here, we delineate the conditions under which the axisymmetric ($n = 0$) instability has the largest growth rate, and the conditions under which the non-axisymmetric instabilities ($n \geq 1$) have the largest growth rate. We will examine the $n = 0, 1, 2, 3$ modes here since we find that $n > 3$ does not dominate for the parameter ranges simulated. When calculating the most dangerous mode, we explore the wavenumber range $0 < k < 3$.

Figure 7 plots which mode has the largest growth rate for different values of the non-dimensional surface tension (Γ), Cahn number (Cn) and line tension parameter (α). Figure 7(a) shows results for a highly compressed vesicle ($\Gamma = -4$), figure 7(b) for a moderately compressed vesicle ($\Gamma = -2$), figure 7(c) for a vesicle under no tension ($\Gamma = 0$) and figure 7(d) for a vesicle under strong tension ($\Gamma = 30$). Under strong compression ($\Gamma = -4$, figure 7a), we see that only the non-axisymmetric modes are dominant ($n \neq 0$). This observation is similar to what is seen for single-component vesicles, although we note that for this value of tension $\Gamma = -4$, only the $n = 1$ and $n = 2$ modes are unstable for the single-component case, while $n = 2$ and $n = 3$ mostly dominate for the multicomponent case. For very small values of the Cahn number (sharp interface), the dominant modes become more non-axisymmetric, a trend that is seen in all four plots here.

When the vesicle is under moderate compression ($\Gamma = -2$, figure 7b) or no compression ($\Gamma = 0$, figure 7c), all modes $n = 0, 1, 2, 3$ can be unstable depending on the value of Cahn number (Cn) and line tension parameter (α). These results are very different than what is seen for single-component vesicles where no modes are unstable at zero tension ($\Gamma = 0$) and only the $n = 1$ mode is unstable at moderate compression ($\Gamma = -2$). It also appears that α plays a more significant role in the mode selection than the highly compressed vesicle case ($\Gamma = -4$, figure 7a).

When the vesicle is under large tension ($\Gamma = 30$, figure 7d), the phase plot looks similar to the zero-tension case, except that a larger portion of the phase space shows axisymmetric modes ($n = 0$) being dominant. When the tension becomes very large ($\Gamma \rightarrow \infty$), one will only observe pearling modes, recovering the results from the single-component case.

We note that while this analysis shows phase plots for the most unstable modes, it does not comment on the magnitude of these growth rates compared with other modes. Below, we will see that in many situations, the growth rates of different modes can be comparable. When this is the case, mode mixing can arise in nonlinear simulations (discussed in § 6).

Figure 8 presents the magnitude of the most unstable growth rates for the three modes $n = 0, 1, 2$ with respect to the isotropic membrane tension Γ . The dimensionless parameters $\lambda = 1$, $\alpha = 1$, $\beta = 0.5$ and $Pe = 10$ are chosen to be representative of the experimental values of Yanagisawa *et al.* (2010) (see § 6.2 for more details). Based on the interface width between the ordered and disordered phases, we could have different values of the Cahn number. We pick two values here: $Cn = 0.65, 1$. We observe that for lower Cahn numbers ($Cn = 0.65$), the buckling and wrinkling modes dominate over pearling modes at compressive values of membrane tension. As the tension increases, the growth rates become comparable for pearling and buckling. As the Cahn number increases to 1

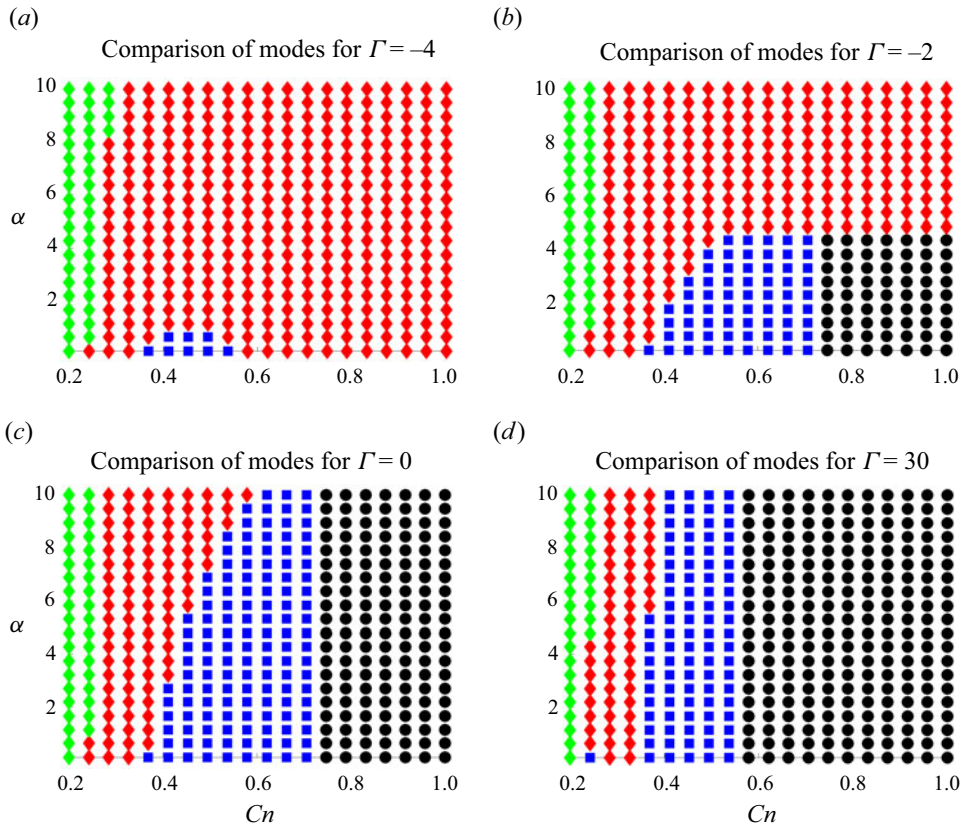


Figure 7. Phase plots for the most dominant mode. The black circles represent the case where $n = 0$ dominates, the blue squares where $n = 1$ dominates, the red diamonds where $n = 2$ dominates and the green diamonds where $n = 3$ dominates. The simulation parameters are $\lambda = 1$, $Pe = 1$, $\beta = 0.5$, $Bq = 0$.

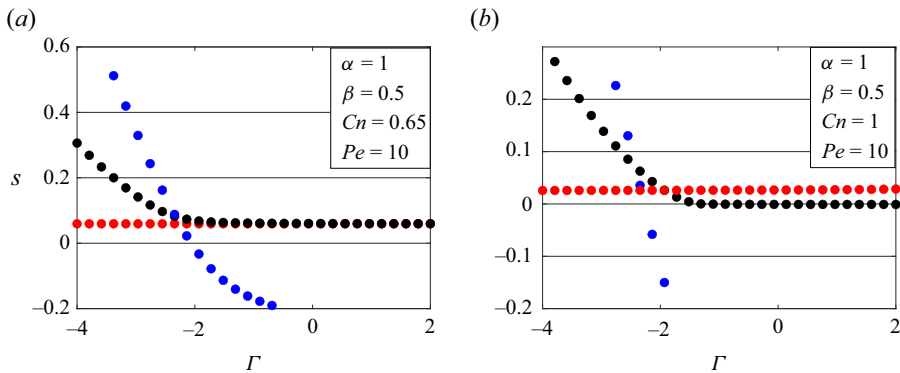


Figure 8. Most unstable growth rates with respect to the isotropic membrane tension Γ for multicomponent vesicles. The red circles represent $n = 0$ pearling modes, black circles represent $n = 1$ buckling modes and blue circles represent $n = 2$ wrinkling modes. The dimensionless parameters are (a) $\lambda = 1$, $Pe = 10$, $\alpha = 1$, $\beta = 0.5$, $Cn = 0.65$, $Bq = 0$ and (b) $\lambda = 1$, $Pe = 10$, $\alpha = 1$, $\beta = 0.5$, $Cn = 1$, $Bq = 0$.

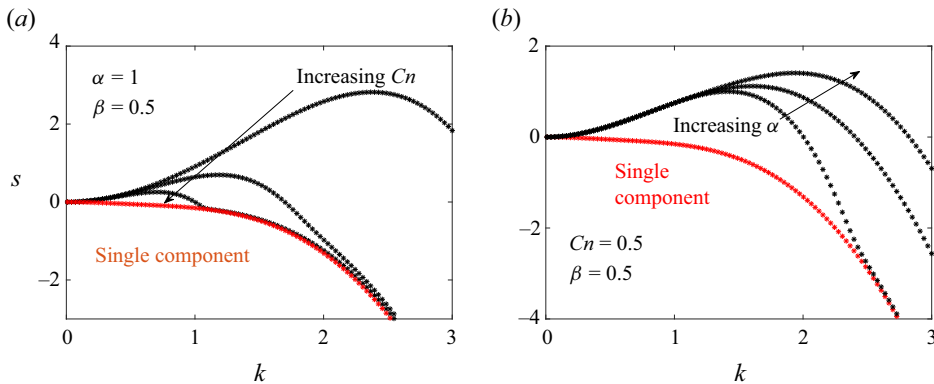


Figure 9. Growth rate (s) versus wavenumber (k) for pearling ($n = 0$) mode. (a) Dependence on Cahn number ($Cn = 0.3, 0.6, 1$) for $\alpha = 1, \beta = 0.5, Pe = 1$. (b) Dependence on line tension parameter ($\alpha = 0.1, 10, 20$) for $Cn = 0.5, \beta = 0.5, Pe = 1$. In both graphs, the multicomponent (black) results are compared against single-component (red) results for $\Gamma = 0, \lambda = 1, Bq = 0$. (a) Variation with Cn and (b) variation with α .

(figure 8b), the wrinkling and buckling modes dominate for highly compressive tensions ($\Gamma < -2$), but become stabilized for small compressive and positive values of Γ , where the pearling modes become dominant. This leads to pure pearling instabilities that will be discussed in detail in § 6.2.

5.3. Wavenumber dependence of growth rates

Figures 9–11 plot the wavenumber dependence of the growth rates for different instabilities – the pearling mode ($n = 0$, figure 9), buckling mode ($n = 1$, figure 10) and wrinkling mode ($n = 2$, figure 11). In these plots, the membrane tension is $\Gamma = 0$. Generally, we observe the following trends: as the Cahn number Cn increases and the line tension parameter α decreases, the maximum growth rate decreases and the most dangerous wavenumber decreases (i.e. the wavenumber k corresponding to the maximum growth rate). These trends occur because large Cn and small α values correspond to large line tensions, which suppresses growth rates and disfavours short wavelength (i.e. large k) instabilities. We note that the extent to which the growth rates are altered depends greatly on the mode number (n) – this is why for certain values of (α, Cn) , the pearling modes have the largest growth rate, but for other values, the non-axisymmetric modes have the largest growth rate. We also see that while large Cn and small α values suppress short wavelength (i.e. $k > 1$) instabilities, Cn plays a more significant role in altering the low wavenumber ($k < 1$) growth rates compared with α .

Some of our trends seem consistent with previous simulations of non-tubular vesicles (Gera 2017). Specifically, the cited study found that increasing α forms shorter wavelength (larger k) stripes on the vesicle, consistent with our study. However, Gera finds that as α rises, it appears that the time slows down to reach the observed behaviour, which is opposite of the growth rate trends observed here (see figures 9b–11b). We point the reader to several caveats: first, the study by Gera inspects non-tubular vesicles, which is different than the geometry considered here. Second, the study examines the full nonlinear dynamics, whereas this section inspects the linearized dynamics and hence the onset of instabilities. Section 6 will provide some results for a weakly nonlinear analysis and compare the results to the linear theory.

Lastly, we inspect the variation of the most unstable wavenumber with respect to the membrane tension Γ for different modes $n = 0, 1, 2$ at the experimentally realizable

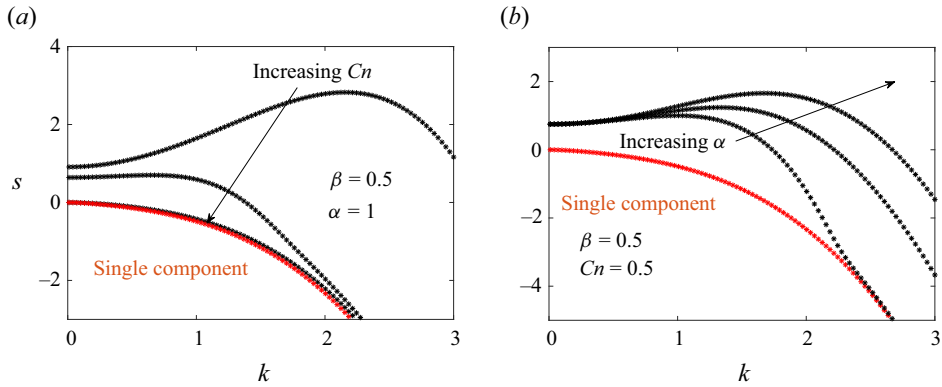


Figure 10. Growth rate (s) versus wavenumber (k) for buckling ($n = 1$) mode. (a) Dependence on Cahn number ($C_n = 0.3, 0.6, 1$) for $\alpha = 1, \beta = 0.5, Pe = 1, Bq = 0$. (b) Dependence on line tension parameter ($\alpha = 0.1, 10, 20$) for $C_n = 0.5, \beta = 0.5, Pe = 1, Bq = 0$. In both graphs, the multicomponent (black) results are compared against single-component (red) results for $\Gamma = 0, \lambda = 1$. (a) Variation with C_n and (b) variation with α .

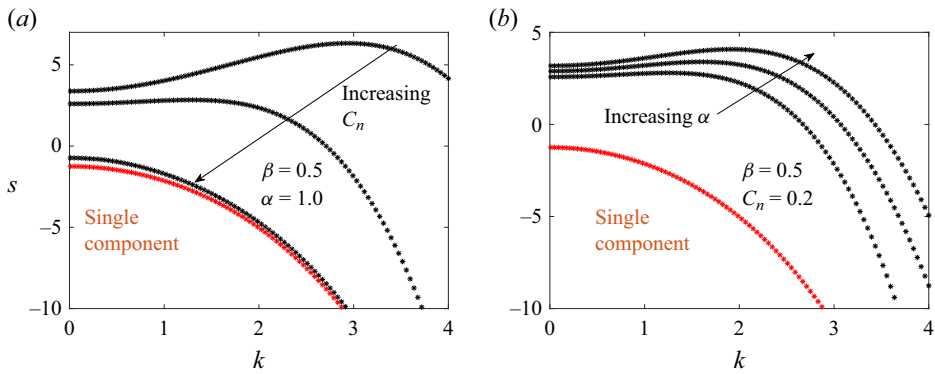


Figure 11. Growth rate (s) versus wavenumber (k) for wrinkling ($n = 2$) mode. (a) Dependence on Cahn number ($C_n = 0.2, 0.3, 0.6$) for $\alpha = 1, \beta = 0.5, Pe = 1, Bq = 0$. (b) Dependence on line tension parameter ($\alpha = 0.1, 10, 20$) for $C_n = 0.2, \beta = 0.5, Pe = 1, Bq = 0$. In both graphs, the multicomponent (black) results are compared against single-component (red) results for $\Gamma = 0, \lambda = 1$. (a) Variation with C_n and (b) variation with α .

ranges of parameters. Since this variation is not large, we have added these plots to the [Appendix](#) (see § A.5).

5.4. Effect of Péclet number on instability

In [figure 12](#), we explore the effect of Pe on the growth rates of instabilities. From (3.18), we can see that the Pe does not alter the onset of instability (determined by the right-hand side of that equation). However, it heavily influences the growth rate of the most unstable mode. We choose a particular set of values $\alpha = 1, C_n = 0.65, Bq = 1, \Gamma = 2, \lambda = 1$ and vary the Pe over a wide range since it is governed by the average bending stiffness (k_0), viscosity (μ), mobility of phospholipids (ν) and the size (R). From previous experiments (Yanagisawa *et al.* 2010), we see that $R \sim O(1-10) \mu\text{m}$. This sets the $Pe \sim O(10-100), C_n \sim O(0.1-1), \alpha \sim O(1)$. At experimentally relevant conditions, as discussed in § 6.2, $Pe \sim O(100)$ and the bending time scale is $t_b = \mu R^3 / k_0 \sim 0.01 \text{ s}$,

Stability of cylindrical, multicomponent vesicles

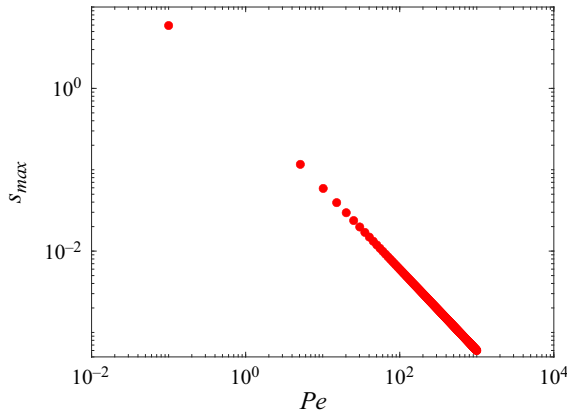


Figure 12. Dependence of the most unstable growth rate on Péclet number $Pe = k_0/\nu\mu R$. The other values are $\alpha = 1$, $\beta = 0.5$, $Cn = 0.65$, $Bq = 1$, $\Gamma = 2$, $\lambda = 1$.

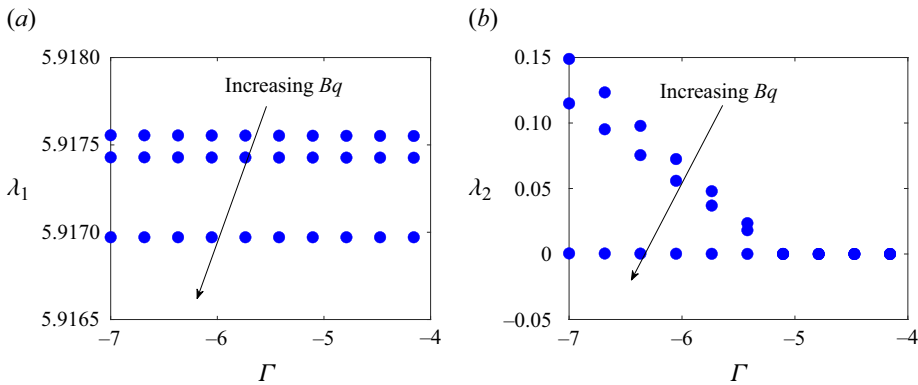


Figure 13. Pearling mode ($n = 0$) eigenvalues corresponding to (3.18) at the most dangerous wavevector k_{max} . The parameters are $\alpha = 1$, $\beta = 0.5$, $Pe = 0.1$, $Cn = 0.65$, $a = -1$, $b = 1$. We choose $Bq = 0.1, 1, 1000$.

which implies that the coarsening time scale $t_{coarsen} = R^2/\nu \sim 1$ s. At these Pe values, the coarsening dynamics decides the magnitude of growth rate, which gives rise to the $s_{max} \sim Pe^{-1}$ scaling in figure 12.

5.5. Effect of surface viscosity and general condition for instability

Surface viscosity is a fundamental parameter that affects dynamics of vesicles significantly. One study is worth mentioning here since it pertains to the effect of surface viscosity on the dynamics of vesicles and curved surfaces (Ambruş *et al.* 2019). The authors considered inertial dynamics driven by convective coarsening in the system.

To understand the effect of Bq , we did the following. For a given value of planar wavenumber n ($n = 0, 1$), we found the most dangerous wavenumber k_{max} that yields the largest growth rate. For this wavenumber k_{max} , there are two eigenvalues and eigenvectors associated with the 2×2 linear system in (3.18) – one that corresponds to the most dangerous mode (λ_1) and another that is subdominant (λ_2). We plot the eigenvalues (λ_1, λ_2) corresponding to $n = 0$ and $n = 1$ in figures 13 and 14, respectively. The main observation that can be made is that λ_2 is largely suppressed as Bq increases, whereas

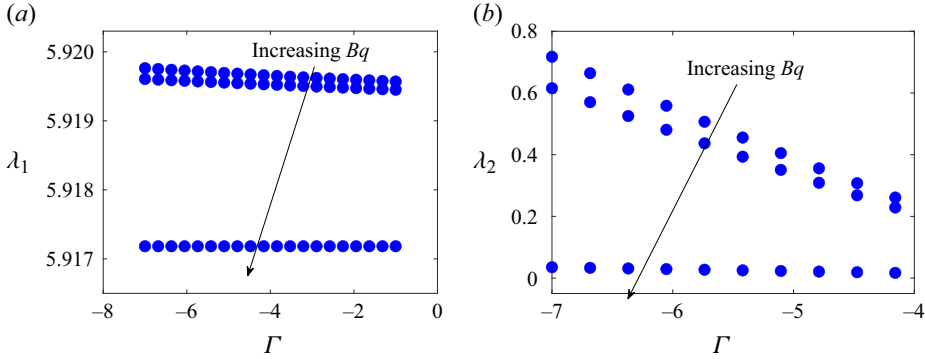


Figure 14. Buckling mode ($n = 1$) eigenvalues corresponding to (3.18) at the most dangerous wavevector k_{max} . The parameters are $\alpha = 1, \beta = 0.5, Pe = 0.1, Cn = 0.65, a = -1, b = 1$. We choose $Bq = 0.1, 1, 1000$.

the most dangerous mode λ_1 is largely unaffected. The behaviour of the subdominant eigenvalue λ_2 is similar to the behaviour seen in single-component vesicles. We believe the reason for these observations is the following: the eigenvector $[r_{kn}, q_{kn}]$ corresponding to λ_2 tends to have a larger component in the shape (r_{kn}) direction compared with the concentration (q_{kn}) direction. The Boussinesq number Bq primarily affects the shape dynamics r_{kn} as it appears in the term Λ_{kn} in (3.18), but plays a smaller role in the q_{kn} dynamics.

A limit often relevant in the case of two-dimensional (2-D) hydrodynamics corresponds to $Bq \rightarrow \infty$. This case has been explored by Bachini *et al.* (2023b), where they considered the Saffman–Delbruck length to be $l_{SD} \rightarrow \infty$. In this limit, we expect that the dynamics would be governed by the mixing terms M_{kn}, V_{kn} in (3.17). This would be very similar to the surface Cahn–Hilliard equation on curved surfaces as explored by the authors.

To conclude this discussion, we leave the reader with a more general condition for stability. From (3.18), we can evaluate the condition for instability to be

$$\det \begin{bmatrix} L_{kn} & M_{kn} \\ M_{kn} & V_{kn} \end{bmatrix} < 0. \tag{5.1}$$

This gives us

$$\left[\Gamma(n^2 + k^2 - 1) + \frac{3}{2} + 2k^2 + (n^2 + k^2) \left(n^2 + k^2 - \frac{5}{2} \right) \right] [\tilde{a} + Cn^2(n^2 + k^2)] < \alpha\beta Cn^2(n^2 + k^2 - 1)^2. \tag{5.2}$$

Based on the choice of $\tilde{a}, Cn, \Gamma, \alpha, \beta$, we can generate the set of unstable pairs of n, k . Note that from the above analysis, there are situations where a vesicle that would otherwise be stable in the absence of coupling (i.e. $\beta = 0, L_{kn}, V_{kn} > 0$) is unstable when coupling is present ($\beta \neq 0$). Figure 22 in § A.6 gives an example of this situation.

5.6. Energy analysis

There are three energetic contributions to the instability: bending energy, phase energy and surface tension energy (see § 2.1). To understand which contributions play the largest

Stability of cylindrical, multicomponent vesicles

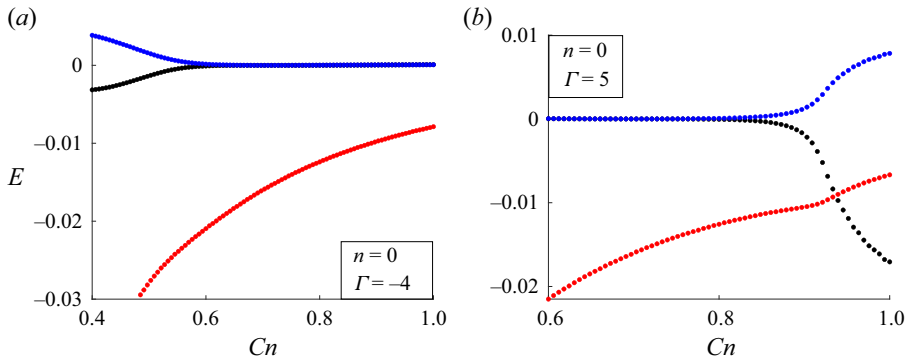


Figure 15. Energetic contributions to the pearling mode ($n = 0$) for different values of Cn and Γ . The red circles represent phase energy (ΔE_p), blue circles represent the bending energy (ΔE_b) and the black circles represent the surface tension energy (ΔE_σ). The parameters are $\lambda = 1$, $Pe = 3$, $\alpha = 1$, $\epsilon = 0.1$, $Bq = 0$. (a) $\Gamma = -4$ and (b) $\Gamma = 5$.

role, we perform the following analysis. We take the base state of the cylindrical vesicle ($r_0 = 1$, $q_0 = 0$), and perturb the radius and concentration as follows:

$$r = 1 + \epsilon r_{kn} \cos(kz + n\phi) - \frac{1}{4}\epsilon^2 r_{kn}^2, \quad (5.3)$$

$$q = \epsilon q_{kn} \cos(kz + n\phi) - \frac{1}{2}\epsilon^2 q_{kn} r_{kn}. \quad (5.4)$$

The higher order terms are present to conserve the volume and order parameter to $O(\epsilon^2)$: i.e. $V = V_0$ and $\int q dS = 0$. We then compute the change in energy between the perturbed and base states, and break them into the bending (b), phase (p) and surface tension (σ) contributions:

$$\Delta E = E(r_{kn}, q_{kn}) - E(r_{kn} = 0, q_{kn} = 0) \quad (5.5)$$

$$= \Delta E_b + \Delta E_p + \Delta E_\sigma. \quad (5.6)$$

If $\Delta E < 0$, the perturbation has a lower energy than the base state, which leads to instability. If $\Delta E > 0$, the perturbation has a higher energy than the base state, and thus the base state is locally stable. Below are the bending, phase and surface tension contributions to the energy change per unit length of the vesicle. The algebraic details are given in § A.7.

$$\Delta E_b = \frac{\pi\epsilon^2 r_{kn}^2}{2} \left(2k^2 + (k^2 + n^2) \left(k^2 + n^2 - \frac{5}{2} \right) + \frac{3}{2} \right) + \beta\pi\epsilon^2 r_{kn} q_{kn} (k^2 + n^2 - 1), \quad (5.7)$$

$$\Delta E_p = \frac{\pi\epsilon^2 q_{kn}^2}{2\alpha Cn^2} [\tilde{a} + Cn^2(n^2 + k^2)], \quad (5.8)$$

$$\Delta E_\sigma = \frac{\Gamma\pi\epsilon^2 r_{kn}^2}{2} (n^2 + k^2 - 1). \quad (5.9)$$

In figure 15, we examine the energetic contributions to the pearling ($n = 0$) mode at $\lambda = 1$, $Pe = 3$, $\alpha = 1$. Here, we use the linear stability theory to compute the dominant eigenvector $[r_{kn}, q_{kn}]$ at the most unstable wavenumber k , and then compute the energetic contributions (ΔE_b , ΔE_p , ΔE_σ) as stated above for perturbation value $\epsilon = 0.1$. We vary the value of Cn while keeping Γ fixed at -4 and 5 , both representing extremes of

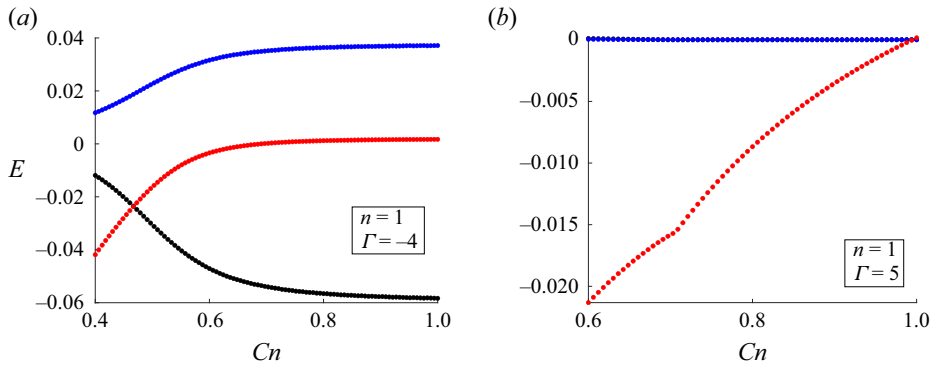


Figure 16. Energetic contributions to the buckling mode ($n = 1$) for different values of Cn and Γ . The red circles represent phase energy (ΔE_p), blue circles represent the bending energy (ΔE_b) and the black circles represent the surface tension energy (ΔE_σ). The parameters are $\lambda = 1$, $Pe = 3$, $Bq = 0$, $\alpha = 1$, $\epsilon = 0.1$. (a) $\Gamma = -4$ and (b) $\Gamma = 5$.

compression and tension, respectively. It can be seen that for experimentally relevant values of the Cahn number Cn , the phase energy is the primary driver for the destabilization of the vesicle shape for highly compressive values of Γ (figure 15a). The bending energy seems to have a stabilizing effect on the vesicle pearling whereas the tension has a weakly destabilizing effect. When the value of Γ is largely positive, as the Cn increases, the tension energy begins destabilizing the vesicle more than the phase energy whereas the bending energy is always stabilizing (figure 15b).

In figure 16, we examine the energetic contributions to the buckling ($n = 1$) mode at $\lambda = 1$, $Pe = 3$, $\alpha = 1$. We vary the value of Cn while keeping Γ fixed at -4 and 5 , both representing extremes of compression and tension, respectively. It can be seen that for experimentally relevant values of the Cahn number Cn , for highly compressive values of Γ , the tension energy causes the largest destabilization of the vesicle shape as the Cn increases whereas the phase energy contributes less (figure 16a). The bending energy seems to have a stabilizing effect on the buckling. When the value of Γ is largely positive (figure 16b), we see that the phase energy is the primary driver for the destabilization of the vesicle shape.

6. Weakly nonlinear analysis

6.1. Solving nonlinear equations

We perform a weakly nonlinear stability analysis on the base state mentioned in § 3.1. We perturb all geometric and physical quantities an infinitesimal amount $\epsilon \ll 1$ as shown below:

$$r = 1 + \epsilon \sum_{kn} r_{kn} \exp(ikz + in\phi), \tag{6.1a}$$

$$\sigma = \Gamma + \epsilon \sum_{kn} \sigma_{kn} \exp(ikz + in\phi), \tag{6.1b}$$

$$\mathbf{u}^{in/out} = \epsilon \sum_{kn} \mathbf{u}_{kn}^{in/out} \exp(ikz + in\phi), \tag{6.1c}$$

$$q = \epsilon \sum_{kn} q_{kn} \exp(ikz + in\phi), \quad (6.1d)$$

$$p^{in} = \Gamma - \frac{1}{2} + \epsilon \sum_{kn} p_{kn}^{in} \exp(ikz + in\phi), \quad (6.1e)$$

$$p^{out} = \epsilon \sum_{kn} p_{kn}^{out} \exp(ikz + in\phi). \quad (6.1f)$$

To understand the coarsening dynamics more quantitatively, we solve the linearized shape equation ((3.17)) along with the Cahn–Hilliard equation given by

$$\begin{aligned} \frac{dq_{kn}}{dt} = & -\frac{\mathcal{F}(\mathbf{u} \cdot \nabla_s q)}{Pe} - \frac{(n^2 + k^2)}{Pe} [\tilde{a} + Cn^2(n^2 + k^2)]q_{kn} - \frac{\tilde{b}(n^2 + k^2)}{Pe} \mathcal{F}(q^3) \\ & - \alpha\beta Cn^2(n^2 + k^2)(n^2 + k^2 - 1)r_{kn}. \end{aligned} \quad (6.2)$$

The equation above is the same as (3.2), except that two nonlinearities are added: a convective term $-\mathcal{F}(\mathbf{u} \cdot \nabla_s q)/Pe$ and the chemical potential from the quartic portion of the free energy $-(\tilde{b}(n^2 + k^2)/Pe)\mathcal{F}(q^3)$, where $\mathcal{F}(\dots)$ represents a Fourier transform. Keeping the entire quartic potential in the Cahn–Hilliard equation allows the concentration and shape fields to evolve to an equilibrium state. We emphasize that we solve the full Cahn–Hilliard equations in the small deformation limit by retaining the nonlinear convective and quartic potential terms. The numerical procedure is mentioned in § A.8.

In figure 17, we perform a one-to-one comparison of linear and nonlinear simulations from the same initial condition, to understand when these two simulations start deviating from each other. In this figure, based on the parameters mentioned in the caption, the linear stability analysis predicts most unstable growth rates to be $s_{max} = 0.04152$ for $n = 0$, $s_{max} = 0.04237$ for $n = 1$, $s_{max} = 0.02977$ for $n = 2$. According to these values, at early times, there should be a mix of buckling, pearling and wrinkling, whereas at longer times, buckling should dominate with some pearling effects. The corresponding nonlinear simulations predict similar dynamics up to $t \sim 250$, which can translate to 12–25 s, beyond which we see buckling dominating with spiral order parameter patterns due to mode-mixing. The time window of matching between the linear and nonlinear dynamics is experimentally relevant and depends heavily on the Pe value. As discussed previously, for higher Pe values, the linear growth rates reduce in magnitude thereby delaying the nonlinear effects. For larger Cn values, the dynamics become comparable over an even longer time window. This comparison is done in figure 18 where we can see that the patterns look similar up to $t \sim 1000$, which corresponds to $t \sim 50$ –100 s. This is an example of the linear theory working well at experimental time scales. Generally, linear and nonlinear dynamics show qualitatively similar shapes and concentration profiles at long times when only one mode is considered to be dominant (e.g. figure 18 where only pearling is the dominant mode for $Cn \geq 0.8$ with the other parameters kept the same as figure 17).

6.2. Experimental comparison

In this section, we compare our nonlinear dynamical simulations with experimental observations from (Yanagisawa *et al.* 2010). In this paper, the authors explored periodic modulations in cylindrical, multicomponent vesicles containing DOPC/DPPC/cholesterol at 1 : 1 DOPC :: DPPC and different amounts of cholesterol. The vesicles were created

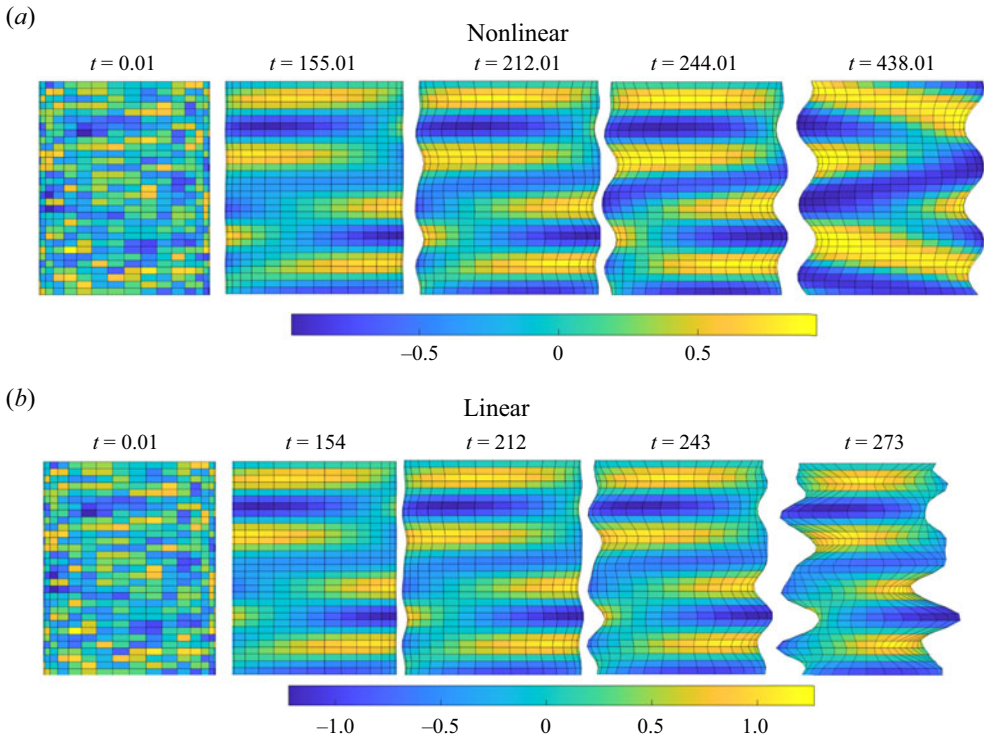


Figure 17. Linear versus nonlinear simulations for $\alpha = 1$, $\beta = 0.5$, $\Gamma = 2$, $a = -1$, $b = 1$, $Cn = 0.45$, $Pe = 30$, $Bq = 1$. The initial condition is $r = 1$, $q = \epsilon(2 \times \text{rand} - 1)$ on a 32×32 grid where $z \in [-10, 10]$, $\phi \in [0, 2\pi]$, with both simulations using the same seed in random number generation. The time step size is $\Delta t = 0.01$ and $\epsilon = 0.001$. The colourbar represents the value of $q/|q|$. The nonlinear simulation video (figure 17a) is given in Movie 4 of the supplementary movies at <https://doi.org/10.1017/jfm.2024.1120>.

by taking spherical giant unilamellar vesicles (GUVs) with these lipids, and osmotically deflating them to create tubular shapes of radius $R \approx 0.5\text{--}3 \mu\text{m}$ with aspect ratios between $L = 5$ and 20 . The modulations observed arose due to the phase separation into liquid-ordered (L_o) and liquid-disordered (L_d) phases, similar to what is seen in our theories. The interior and exterior fluids were the same (up to the sugars used for osmotic deflation), yielding a viscosity ratio $\lambda \approx 1$. Based on the ratios of DOPC : DPPC : Chol in their studies, the average bending stiffness was estimated to be $k_0 \approx 10^{-19} \text{ J}$ and the difference in bending stiffness between domains varied in the range $\beta = 0.1\text{--}0.5$. The line tension was estimated to be roughly 1 pN , yielding a line tension parameter $\alpha \approx 1$. Examining the interface width yields a Cahn number $Cn = \epsilon^{\text{width}} / (\sqrt{2}R) \approx 0.3\text{--}1$. We find that results are highly sensitive to this parameter as shown below. The Péclet number was estimated to be $Pe = O(10)\text{--}O(100)$ based on limited data of lipid diffusivities (Negishi *et al.* 2008).

The only non-dimensional number we were not able to infer from experimental data was the dimensionless surface tension $\Gamma = \sigma_0 R^2 / k_0$, since the surface tension σ_0 was not provided. In principle, one could obtain σ_0 by performing an equilibrium simulation of vesicle shape since this quantity arises as a Lagrange multiplier that enforces the constant area of the membrane. However, this simulation is quite difficult to do for highly deflated, multicomponent vesicles (and to our knowledge has yet to be performed). Instead, we make

Stability of cylindrical, multicomponent vesicles

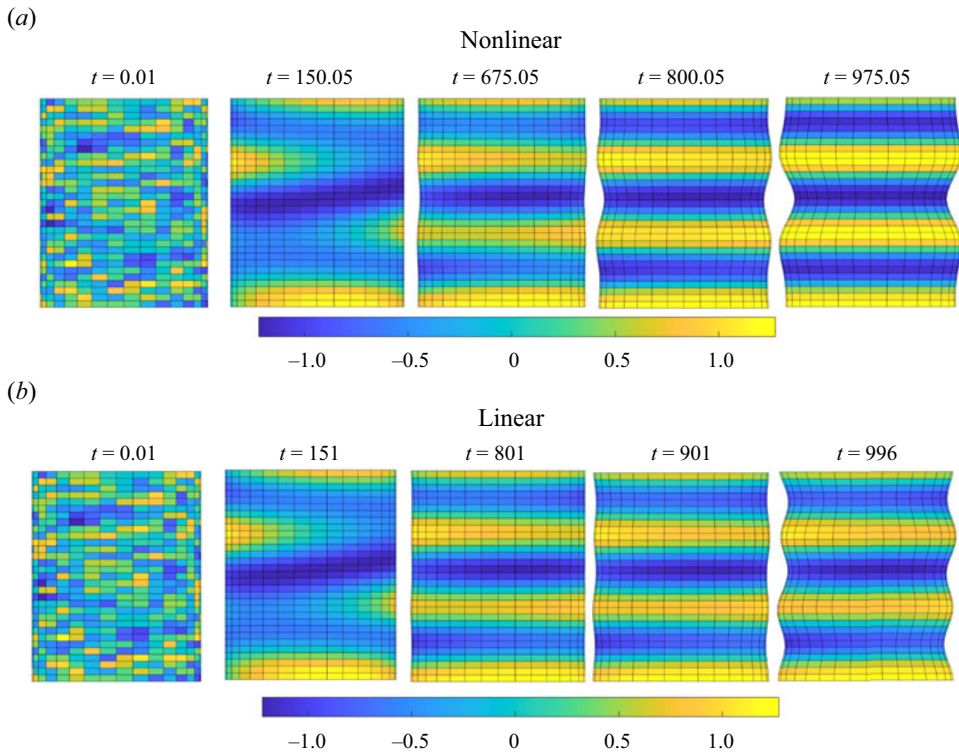


Figure 18. Linear versus nonlinear simulations for $\alpha = 1$, $\beta = 0.5$, $\Gamma = 2$, $a = -1$, $b = 1$, $Cn = 0.8$, $Pe = 30$, $Bq = 1$. The initial condition is $r = 1$, $q = \epsilon(2 \times \text{rand} - 1)$ on a 32×32 grid where $z \in [-10, 10]$, $\phi \in [0, 2\pi]$, with both simulations using the same seed in random number generation. The time step size is $\Delta t = 0.01$ and $\epsilon = 0.001$. The colourbar represents the value $q/|q|$. The nonlinear simulation video (figure 18a) is given in Movie 3 of the supplementary movies.

a note that σ_0 is likely to be very small since the vesicles are under no external force, and for values $\sigma_0 = 10^{-7} \text{ N m}^{-1}$, this yields $\Gamma \sim O(1)$. Thus, we will perform simulations for several different values of Γ and see how they compare against experimental data. We will also vary Cn since the results are sensitive to this value. For the other parameters, we set $\lambda = 1$, $Pe = 10$, $\alpha = 1$, $\beta = 0.5$, $Bq = 1$ consistent with estimated values listed above. The characteristic time scale using the parameters chosen above corresponds to the bending scale $t_b = \eta R^3/k_0 \approx 0.01 \text{ s}$. In the following results (figures 19 and 20), we simulate the dynamics up to $t \sim 1000$ bending times, which would correspond to $\sim 10 \text{ s}$. From the experimental paper in discussion (Yanagisawa *et al.* 2010), the dynamics are observed over $\sim 45 \text{ s}$. This seems comparable but not exactly accurate. We note that the choice of Pe plays a very important role here. We have assumed the lipid diffusivity to be $\nu = 10^{-11} \text{ m}^2 \text{ s}^{-1}$, but there have been recent studies that have shown this value to be potentially even lower $O(10^{-12} \text{ m}^2 \text{ s}^{-1})$ (Pöhl, Trollmann & Böckmann 2023). In these cases, the Pe could go to 100 for the same set of experimental parameters chosen by us. If this happens, the dynamics would be governed by the coarsening time scale and not the bending time scale. This would reduce the growth rate of our instabilities and could cause the simulation time scale to be comparable to the experimental time scale.

In figure 19, we show one snapshot of an experimental image where the vesicle forms a straight line with pearls. The bright regions represent the disordered L_d phase and the

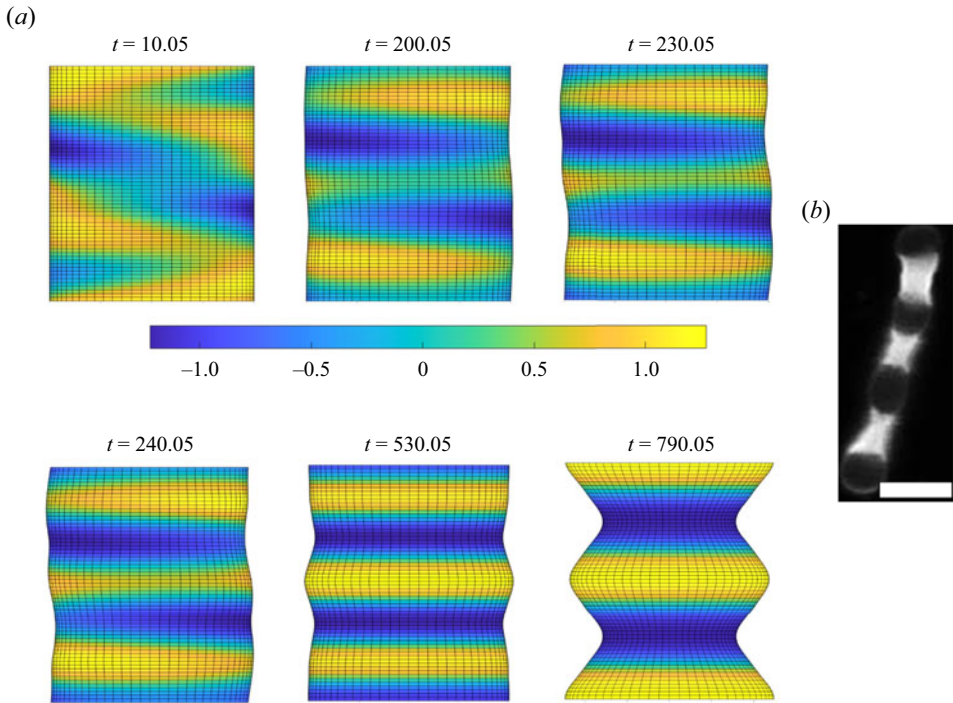


Figure 19. Pearling visual qualitative comparison with experiments (Yanagisawa *et al.* 2010) where the yellow domains represent the cholesterol rich L_o phase (black in experiments) and the blue domains (white in experiments) represent the cholesterol-lacking L_d phase. The parameters for the simulation are $\lambda = 1$, $Pe = 10$, $\alpha = 1$, $\beta = 0.5$, $Bq = 1$, $Cn = 0.8$, and $\Gamma = 0$ corresponding to a vesicle radius $R \approx 1 \mu\text{m}$. The system is simulated up to time $t = 1000$, which translates to a physical time of 10 s. The initial condition is $q = \epsilon(2 * \text{rand} - 1)$ on a 64×64 grid with $z \in [-10, 10]$, $\phi \in [0, 2\pi]$, where $\epsilon = 0.01$. The scale bar represents a length of $5 \mu\text{m}$. The mole fraction ratio of DOPC: DPPC: Chol is 9:9:22. The colourbar represents the value of $q/|q|$. The nonlinear simulation video is given in Movie 2 of supplementary movies. Experimental image is reproduced with permission from Yanagisawa *et al.* (2010).

dark regions represent the ordered L_o phase. The interface width is fairly diffuse, leading to $Cn \approx 0.8$. If we perform nonlinear simulations with no tension $\Gamma = 0$, we observe qualitatively similar behaviour to experiments. These snapshots are shown at various time steps, with similar behaviour also seen for $\Gamma > 0$ (not shown). For the simulated case, the linear stability analysis also predicts pearling shapes like the nonlinear analysis, albeit with a more aggressive growth rate ($s = 0.039$ for linear result, corresponding to time scale $t = 1/s \approx 25$ as opposed to $t \sim O(100)$ for nonlinear simulations). However, if $Pe \geq 50$ (which could be realistic based on the uncertainty for lipid diffusivities), the growth rates from the linear analysis could be comparable to the experimentally relevant time scales $t \sim O(100)$ s.

In the experiments, vesicles occasionally exhibited buckling in addition to pearling. In these situations, the interface width appears sharper than the case when pearls form. Figure 20 shows a snapshot of such an example using nonlinear simulations with a sharper interface $Cn = 0.3$ and slightly positive tension $\Gamma = 2$. The nonlinear simulations at intermediate times show pearling and buckling modes (the corresponding linear stability analysis shows that $s = 0.1802$ for $n = 0$, $s = 0.24$ for $n = 1$ and $s = 0.28$ for $n = 2$, thereby showing buckling, wrinkling and pearling), but at long time, the nonlinear analysis

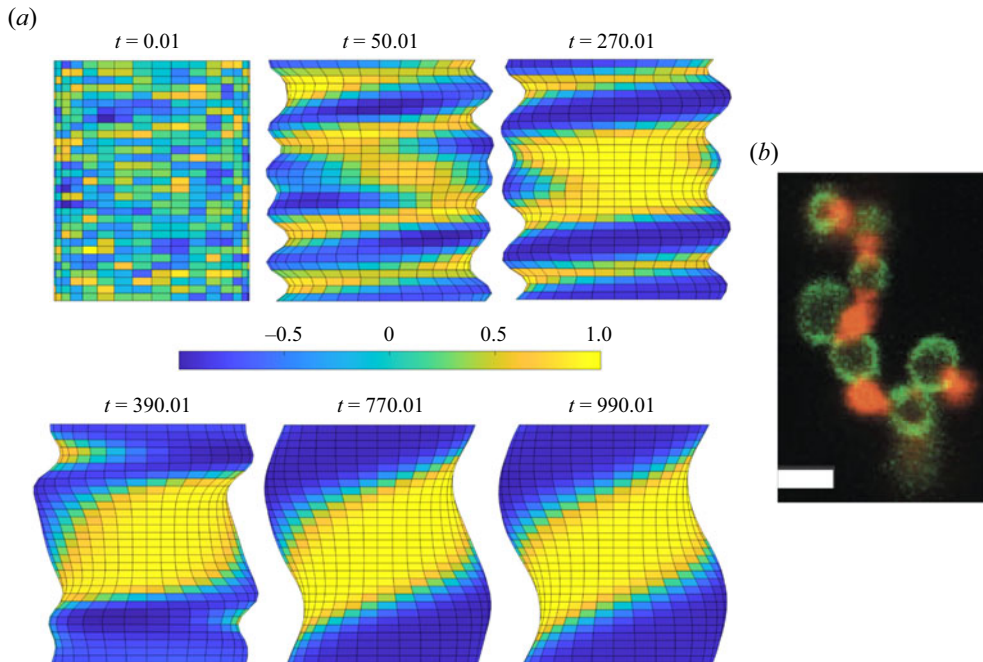


Figure 20. Mixed mode instability found in experiments (Yanagisawa *et al.* 2010) and simulations. The pearling mode ($n = 0$) can have a larger wavenumber compared with the buckling mode ($n = 1$). The parameters for the simulation are $\lambda = 1$, $Pe = 10$, $\alpha = 1$, $Bq = 1$, $\beta = 0.5$, $Cn = 0.3$ and $\Gamma = 2$ corresponding to $R = 1 \mu\text{m}$. The system is simulated up to time $t = 1000$, which translates to a physical time of 10 s. The initial condition is $q = \epsilon(2 * \text{rand} - 1)$ on a 32×32 grid where $z \in [-10, 10]$, $\phi \in [0, 2\pi]$, where $\epsilon = 0.01$. The inset scale bar represents a length of $2 \mu\text{m}$. The mole fraction ratio DOPC : DPPC : Chol is 3 : 3 : 4. The colourbar represents the value of $q/|q| \in [-1, 1]$. The nonlinear simulation video is given in Movie 1 of supplementary files. Experimental image is reproduced with permission from Yanagisawa *et al.* (2010).

shows buckling with a diagonal concentration stripe. The long-wavelength buckling shape appears similar to the experiment, but the short wavelength pearls are not observed. This may be due to the fact that the simulations assume small deformations, which are clearly not followed in experiments. We note that the shape observed in our simulations is sensitive to the initial condition in the simulation. Just like the pearling case, we believe that based on the Pe , the linear dynamics could get delayed thereby giving accurate dynamics at experimentally relevant time scales.

7. Conclusions

We performed linear and nonlinear stability analyses on a tubular vesicle containing multiple components in its bilayer structure. We observed that the vesicle could exhibit pearling, buckling and wrinkling behaviour in multiple regimes of membrane (surface) tension Γ , even at moderate compressive or extensive values, a result that is not seen in single-component vesicles. For the linear stability analysis, we determined the conditions under which axisymmetric and non-axisymmetric modes experience the largest growth rate, as well as characterized the growth rates and the wavenumber selection for each mode. We discussed the role of Péclet number (comparing coarsening and bending time scales), as well as the role of surface viscosity on the instability. Interestingly, in many

situations, the axisymmetric pearling mode ($n = 0$) can have a similar growth rate as the buckling mode ($n = 1$), giving rise to mixed mode dynamics where nonlinear effects could come into play. Lastly, we provided an energy phase diagram to explain the driving forces behind this instability. We saw that there is an interplay between the bending energy, phase energy and the membrane tension energy, and the dominant contribution depends on the surface tension, line tension and bending moduli of the domains.

To understand the nonlinear dynamics more closely, we performed a weakly nonlinear stability analysis where we solve the linear shape dynamics and the fully nonlinear Cahn–Hilliard equation in the weak deformation limit. We observed that the weakly nonlinear dynamics shows similar spatial characteristics as the linear dynamics when one mode is dominant, but vary in the temporal characteristics, primarily due to the nonlinear stabilizing terms in the Cahn–Hilliard equation. When mode-mixing occurs, the linear and nonlinear simulations are comparable for times $t \sim O(100)$ for $Pe \sim O(10)$, but deviate afterwards.

This study brings to light the importance of understanding flow dynamics being coupled with line tension and bending inhomogeneity effects, which opens up a large phase space to be studied. We also note that while the thermodynamic model (Ginzburg–Landau) helps us qualitatively understand some physical phenomena, a detailed use of more complicated models and their dependence on membrane tension and other physical parameters is needed (Wolff, Marques & Thalmann 2011).

Supplementary movies. Supplementary movies are available at <https://doi.org/10.1017/jfm.2024.1120>.

Funding. The authors would like to acknowledge support from National Science Foundation (grant 2147559-CBET).

Declaration of interests. The authors report no conflict of interest.

Author ORCID.

 Vivek Narsimhan <https://orcid.org/0000-0001-7448-4202>.

Appendix

A.1. Differential geometry basics

Let us consider a cylindrical tube with coordinates given by

$$\mathbf{x} = [a(z, \phi) \cos \phi, a(z, \phi) \sin \phi, z]. \quad (\text{A1})$$

Here, the tube radius $r = a(z, \phi)$ is written as follows:

$$a(z, \phi) = 1 + \epsilon f(z, \phi) + \epsilon^2 g, \quad \epsilon \ll 1, \quad (\text{A2})$$

where $f(z, \phi)$ is a small, spatially varying perturbation and g is a constant that ensures conservation of volume to $O(\epsilon^2)$.

Let us define the tangent vectors $\mathbf{x}_\phi = \partial \mathbf{x} / \partial \phi$ and $\mathbf{x}_z = \partial \mathbf{x} / \partial z$, as well as the normal vector $\mathbf{n} = \mathbf{x}_\phi \times \mathbf{x}_z / |\mathbf{x}_\phi \times \mathbf{x}_z|$. The double derivatives are also defined as $\mathbf{x}_{\phi\phi} = \partial^2 \mathbf{x} / \partial \phi^2$, $\mathbf{x}_{\phi z} = \partial^2 \mathbf{x} / \partial \phi \partial z$ and $\mathbf{x}_{zz} = \partial^2 \mathbf{x} / \partial z^2$. After performing these operations, we evaluate the metric tensor \mathbf{g} and curvature tensor \mathbf{B} below:

$$\mathbf{g} = \begin{bmatrix} \mathbf{x}_\phi \cdot \mathbf{x}_\phi & \mathbf{x}_\phi \cdot \mathbf{x}_z \\ \mathbf{x}_z \cdot \mathbf{x}_\phi & \mathbf{x}_z \cdot \mathbf{x}_z \end{bmatrix} \quad \mathbf{B} = - \begin{bmatrix} \mathbf{n} \cdot \mathbf{x}_{\phi\phi} & \mathbf{n} \cdot \mathbf{x}_{\phi z} \\ \mathbf{n} \cdot \mathbf{x}_{z\phi} & \mathbf{n} \cdot \mathbf{x}_{zz} \end{bmatrix}. \quad (\text{A3a,b})$$

The mean and Gaussian curvatures are obtained by the following formulae:

$$2H = \text{Tr}(\mathbf{g}^{-1} \cdot \mathbf{B}) \quad K = \det(\mathbf{g}^{-1} \cdot \mathbf{B}), \quad (\text{A4a,b})$$

Stability of cylindrical, multicomponent vesicles

while the area element for the surface is given below, where J is the surface Jacobian:

$$dS = J d\phi dz; \quad J = \sqrt{\det(\mathbf{g})}. \quad (\text{A5})$$

Up to $O(\epsilon^2)$, the mean curvature and surface Jacobian are

$$2H = 1 - \epsilon \left(f + \frac{\partial^2 f}{\partial \phi^2} + \frac{\partial^2 f}{\partial z^2} \right) + \epsilon^2 \left[f^2 - \frac{1}{2} \left(\frac{\partial f}{\partial z} \right)^2 + \frac{1}{2} \left(\frac{\partial f}{\partial \phi} \right)^2 + 2f \frac{\partial^2 f}{\partial \phi^2} - g \right], \quad (\text{A6})$$

$$J = 1 + \epsilon f + \epsilon^2 \left[g + \frac{1}{2} \left(\frac{\partial f}{\partial z} \right)^2 + \frac{1}{2} \left(\frac{\partial f}{\partial \phi} \right)^2 \right]. \quad (\text{A7})$$

Up to $O(\epsilon)$, the Gaussian curvature is

$$K = -\epsilon \frac{\partial^2 f}{\partial z^2}. \quad (\text{A8})$$

A.2. Rationale behind dimensionless numbers

In this section, we try to clear the air about multiple dimensionless parameters used in previous studies (Camley & Brown 2014; Safran 2018). According to the mentioned studies, the three experimentally measurable parameters that determine the dimensionless variables are the equilibrium concentration split (ϕ_0), line tension (ξ^{line}) and interface width (ϵ^{width}). These dependencies are listed in (2.3) and (2.4).

Moreover,

$$\phi_0 = \sqrt{\frac{-b}{a}}. \quad (\text{A9})$$

These equations give us

$$\gamma^2 a = \frac{9\phi_0^4 (\xi^{line})^2}{8} \quad (\text{A10})$$

and

$$\gamma^2 = \frac{a(\epsilon^{width})^2}{2}. \quad (\text{A11})$$

This gives

$$a = \frac{3\phi_0^2 (\xi^{line})}{2\epsilon^{width}}, \quad (\text{A12})$$

$$\gamma = \sqrt{\frac{3\phi_0^2 \xi^{line} \epsilon^{width}}{4}}. \quad (\text{A13})$$

Using these equations and the definition of Cahn number,

$$Cn = \frac{\gamma}{R\sqrt{\zeta_0}}, \quad (\text{A14})$$

assuming that $\zeta_0 \approx |a|$, we get

$$Cn = \frac{\epsilon^{width}}{\sqrt{2}R}. \quad (\text{A15})$$

A.3. Coefficients for axisymmetric modes

The linear equations in (3.6) admit an analytical solution for axisymmetric modes ($n = 0$). We obtain

$$A_{k0}^{in} = \frac{\dot{r}_{k0}(k^2 + 1)I_1}{k\Psi}, \quad B_{k0}^{in} = 0, \quad C_{k0}^{in} = -\frac{\dot{r}_{k0}(kI_0 - I_1)}{k\Psi}, \quad (\text{A16a-c})$$

$$A_{k0}^{out} = -\frac{\dot{r}_{k0}(k^2 + 1)K_1}{k\mathcal{E}}, \quad B_{k0}^{out} = 0, \quad C_{k0}^{out} = -\frac{\dot{r}_{k0}(kK_0 + K_1)}{k\mathcal{E}}, \quad (\text{A17a-c})$$

where $\Psi = I_1^2 k^2 - I_0^2 k^2 + 2I_0 I_1 k$ and $\mathcal{E} = K_1^2 k^2 - K_0^2 k^2 - 2K_0 K_1 k$.

These equations give rise to

$$\Lambda_{k0} = 2(k^2 + 1) \left[\frac{K_1^2}{\mathcal{E}} - \lambda \frac{I_1^2}{\Psi} \right] - 4Bq. \quad (\text{A18})$$

A.4. Dispersion relationship, low-Péclet-number limit ($Pe \ll 1$)

When $Pe \ll 1$, the coarsening time is much smaller than the bending time scale ($t_{coarsening} \ll t_{bending}$). In this case, a pseudo-steady approximation can be applied where the vesicle at any instance of time has a fixed, inhomogeneous phospholipid distribution on the surface. Mathematically, the term F_{kn} in (3.18) is zero, which yields the concentration distribution $q_{kn} = -(M_{kn}/V_{kn})r_{kn}$. Since $\Lambda_{kn}\dot{r}_{kn} = L_{kn}r_{kn} + M_{kn}q_{kn}$, one obtains the dispersion relation

$$\dot{r}_{kn} = \frac{r_{kn}}{\Lambda_{kn}} \left[L_{kn} - \frac{M_{kn}^2}{V_{kn}} \right]. \quad (\text{A19})$$

To find the marginal wavenumber at which the growth rate is zero, we equate the term in brackets in (A19) to zero, which yields

$$\Gamma(n^2 + k^2 - 1) + 3/2 + 2k^2 + (n^2 + k^2)(n^2 + k^2 - 5/2) - \frac{\alpha Cn^2 \beta^2 (n^2 + k^2 - 1)^2}{Cn^2 (n^2 + k^2) + \tilde{a}} = 0. \quad (\text{A20})$$

We can obtain the marginal wavenumber for each mode $n = 0, 1, 2, \dots$. If we ignore the bending inhomogeneity and line tension by setting $Cn = \beta = 0$, this recovers the single-component vesicle result of Boedec *et al.* (2014). Lastly, if we consider the case where $\tilde{a} = -1$ (see table 2), we find that when $Cn^2 > 1/k^2$, the growth rate is greater for a multicomponent vesicle compared with a single-component vesicle at the same surface tension conditions.

A.5. Most unstable wavenumber dependence on membrane tension

In figure 21, we inspect the variation of the most unstable wavenumber with respect to the isotropic membrane tension. We can see that the most unstable wavenumber follows a gradual change with the membrane tension Γ . The pearling ($n = 0$) and buckling modes ($n = 1$) show a gradual drop in the wavenumber as the membrane tension increases, while the wrinkling wavenumbers show a slight increase with an increase in the membrane tension. The wavenumber behaviour for $n = 0, n = 1$ is consistent with the

Stability of cylindrical, multicomponent vesicles

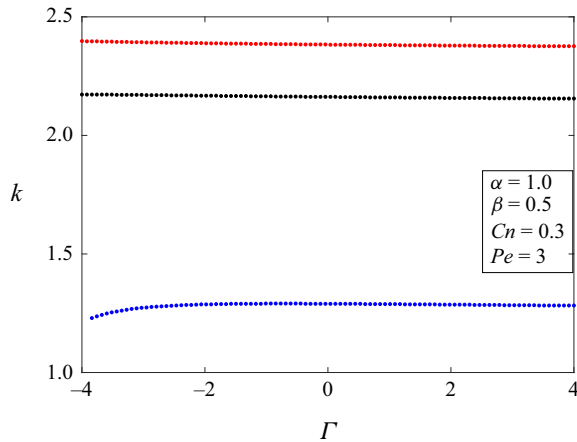


Figure 21. Most unstable wavenumbers with respect to the isotropic membrane tension Γ for single-component vesicles. The red dots represent $n = 0$ pearling modes, black dots represent $n = 1$ buckling modes and blue dots represent $n = 2$ wrinkling modes. In the plot, $\lambda = 1$.

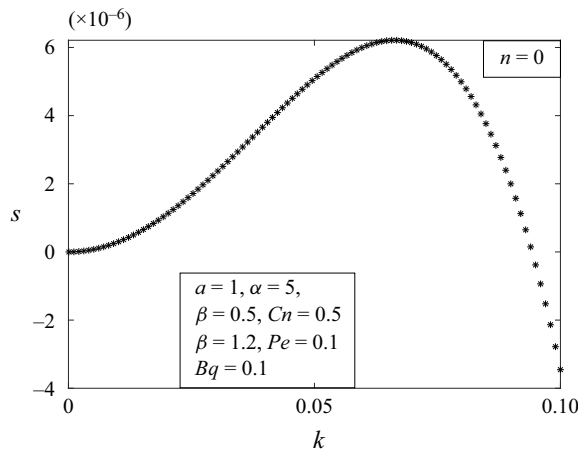


Figure 22. Growth rate variation with wavenumber indicating instability due to coupling ($\beta \neq 0$).

trend for single-component vesicles, albeit a much smaller decline in the magnitude. This indicates that the compressive membrane tension drives a shorter wavelength instability as compared with positive tension values.

A.6. Example when coupling gives rise to instabilities

In [figure 22](#), we can clearly see a case where the coupling between the shape and composition drives the instability on the vesicle surface. With the particular choice of $\Gamma = 1.2$, we know that the $n = 0$ mode is stable for single-component vesicles, whereas $a = 1$ tells us that the Cahn–Hilliard equation would not predict phase separation. However, when $\beta \neq 0$, we see that the growth rate is positive, indicating a coupled instability.

A.7. Derivation of energy change expressions for a deformed cylindrical vesicle

We calculate the energy change of a perturbed vesicle from its unperturbed state, i.e. $\Delta E = E - E[r_{kn}, q_{kn} = 0]$. Without loss in generality, let us write the radius and concentration of the perturbed vesicle as

$$r = 1 + \epsilon r_{kn} \cos(kz + n\phi) - \frac{1}{4}\epsilon^2 r_{kn}^2, \tag{A21}$$

$$q = \epsilon q_{kn} \cos(kz + n\phi) - \frac{1}{2}\epsilon^2 q_{kn} r_{kn}. \tag{A22}$$

The ϵ^2 term is added to the radius so that to $O(\epsilon^2)$, the volume of the vesicle $V = \int \int \frac{1}{2}r^2 d\phi dz$ is equal to its original volume $V_0 = \frac{1}{2} \int \int d\phi dz$. The ϵ^2 term is added to the concentration field so that the order parameter is conserved to $O(\epsilon^2)$ – i.e. $\int q dS = 0$. Using (A5) and (A7), the surface element along the vesicle is given by $dS = J d\phi dz$, with the surface Jacobian given by

$$J = 1 + \epsilon r_{kn} \cos(kz + n\phi) + \frac{\epsilon^2 r_{kn}^2}{4} [n^2 + k^2 - 1 - (n^2 + k^2) \cos(2kz + 2n\phi)]. \tag{A23}$$

The energy contribution from surface tension is

$$E_\sigma = \Gamma \int dS. \tag{A24}$$

We perform the above integration, noting that only the zeroth-order harmonics (i.e. constant terms) contribute to the integral. This yields an energy change per unit length

$$\Delta E_\sigma = \frac{\Gamma \pi \epsilon^2 r_{kn}^2}{2} (n^2 + k^2 - 1). \tag{A25}$$

The energy contribution from the phase behaviour is given by the Landau–Ginzberg model. In dimensionless form, it is

$$E_p = \frac{1}{Cn^2\alpha} \int \frac{\tilde{a}}{2}|q|^2 + \frac{\tilde{b}}{4}|q|^4 + \frac{Cn^2}{2} |\nabla_s q|^2 dS. \tag{A26}$$

We drop the middle term since it is $O(\epsilon^4)$ while

$$|\nabla_s q|^2 = \frac{(n^2 + k^2)\epsilon^2 q_{kn}^2}{2} [1 - \cos(2kn + 2n\phi)]. \tag{A27}$$

The energy change per unit length in this case is

$$\Delta E_p = \frac{\pi \epsilon^2 q_{kn}^2}{2\alpha Cn^2} [\tilde{a} + Cn^2(n^2 + k^2)]. \tag{A28}$$

The Canham–Helfrich bending energy is given by

$$E_b = \int 2(1 + \beta q)|H|^2 dS = \int 2|H|^2 dS + \int 2\beta q|H|^2 dS. \tag{A29}$$

Stability of cylindrical, multicomponent vesicles

The first integral in (A29) is the same as that for a single-component cylindrical vesicle (Narsimhan 2014), while the second integral gives a coupled energy term. The expressions are

$$\Delta E_b = \frac{\pi \epsilon^2 r_{kn}^2}{2} \left(2k^2 + (k^2 + n^2) \left(k^2 + n^2 - \frac{5}{2} \right) + \frac{3}{2} \right) + \beta \pi \epsilon^2 r_{kn} q_{kn} (k^2 + n^2 - 1). \quad (\text{A30})$$

Lastly, we make a comment on the total change in free energy. If we examine (A25), (A28) and (A30), we see that the total change in energy takes a quadratic form $\Delta E_{tot} = \frac{1}{2} \mathbf{y}^T \cdot \mathbf{E} \cdot \mathbf{y}$, where $\mathbf{y} = \epsilon [r_{kn}, q_{kn}]^T$ and \mathbf{E} is

$$\mathbf{E} = \frac{1}{\epsilon^2} \begin{bmatrix} \frac{\partial^2 \Delta E_{tot}}{\partial r_{kn} \partial r_{kn}} & \frac{\partial^2 \Delta E_{tot}}{\partial r_{kn} \partial q_{kn}} \\ \frac{\partial^2 \Delta E_{tot}}{\partial q_{kn} \partial r_{kn}} & \frac{\partial^2 \Delta E_{tot}}{\partial q_{kn} \partial q_{kn}} \end{bmatrix} = \pi \begin{bmatrix} L_{kn} & M_{kn} \\ M_{kn} & V_{kn} \end{bmatrix}. \quad (\text{A31})$$

Thus, the matrices L_{kn} , M_{kn} and V_{kn} in the linear stability analysis are related to the second variation in the free energy. The quantity, $(1/\pi)(\partial \Delta E_{tot} / \partial \epsilon r_{kn})$ gives the linearized, normal tractions on the interface (see (2.9)), while the $(1/\pi)(\partial \Delta E_{tot} / \partial \epsilon q_{kn})$ gives the chemical potential on the interface (see (2.12)). Thus, the energy analysis is consistent with the linear stability analysis, although the energy analysis cannot give information on the time scale of instability or the most dangerous wavenumber.

A.8. Numerical procedure for weakly nonlinear analysis

From (3.17) and (A33), we have the following:

$$\Lambda_{kn} \dot{r}_{kn} = L_{kn} r_{kn} + M_{kn} q_{kn}, \quad (\text{A32})$$

$$\begin{aligned} \frac{dq_{kn}}{dt} = & -\frac{\mathcal{F}(\mathbf{u} \cdot \nabla_s q)}{Pe} - \frac{(n^2 + k^2)}{Pe} [\tilde{a} + Cn^2(n^2 + k^2)] q_{kn} - \frac{\tilde{b}(n^2 + k^2)}{Pe} \mathcal{F}(q^3) \\ & - \alpha \beta Cn^2(n^2 + k^2)(n^2 + k^2 - 1) r_{kn}. \end{aligned} \quad (\text{A33})$$

For (3.17), we use a first-order Euler method with an implicit scheme for the shape term and an explicit scheme for the order parameter term to provide additional stability. If we pick the i th time step along with Δt as the step size, we get

$$\Lambda_{kn} \left(\frac{r_{kn}^{i+1} - r_{kn}^i}{\Delta t} \right) = L_{kn} r_{kn}^{i+1} + M_{kn} q_{kn}^i, \quad (\text{A34})$$

$$r_{kn}^{i+1} = \frac{\left(r_{kn}^i + \Delta t \frac{M_{kn}}{\Lambda_{kn}} q_{kn}^i \right)}{1 - \Delta t \Lambda_{kn}}. \quad (\text{A35})$$

Using this information of the shape deformation at the $(i + 1)$ th time step, we discretize the Cahn–Hilliard equation using a splitting scheme mentioned by Yoon *et al.* (2020),

$$\begin{aligned} \frac{q_{kn}^{i+1} - q_{kn}^i}{\Delta t} = & -\frac{F_{kn}^i}{Pe} - \frac{(n^2 + k^2)}{Pe} C_{kn}^i - \frac{2(n^2 + k^2)}{Pe} q_{kn}^{i+1} - \frac{Cn^2(n^2 + k^2)^2}{Pe} q_{kn}^{i+1} \\ & - \alpha \beta Cn^2(n^2 + k^2)(n^2 + k^2 - 1) r_{kn}^{i+1}, \end{aligned} \quad (\text{A36})$$

where $F_{kn}^i \equiv \mathcal{F}(\mathbf{u}^i \cdot \nabla_s q^i)$ and $C_{kn}^i \equiv \mathcal{F}((\tilde{a} - 2)q^i + \tilde{b}(q^i)^3)$

$$q_{kn}^{i+1} = \frac{q_{kn}^i - \frac{\Delta t}{Pe} F_{kn}^i - \frac{\Delta t(n^2 + k^2)}{Pe} C_{kn}^i - \frac{\Delta t \alpha C n^2 \beta (n^2 + k^2)(n^2 + k^2 - 1)}{Pe} r_{kn}^{i+1}}{1 + \frac{\Delta t}{Pe} (2(n^2 + k^2) + C n^2 (n^2 + k^2)^2)}.$$

(A37)

By solving for r_{kn}^{i+1} , q_{kn}^{i+1} , we can evolve in time to obtain the shape and order parameter evolution.

REFERENCES

- ABREU, D., LEVANT, M., STEINBERG, V. & SEIFERT, U. 2014 Fluid vesicles in flow. *Adv. Colloid Interface Sci.* **208**, 129–141.
- AGRAWAL, A. & STEIGMANN, D.J. 2011 A model for surface diffusion of trans-membrane proteins on lipid bilayers. *Z. Angew. Math. Phys.* **62**, 549–563.
- ALMEIDA, P.F.F. 2009 Thermodynamics of lipid interactions in complex bilayers. *Biochim. Biophys. Acta Biomembr.* **1788**, 72–85.
- AMAZON, J.J., GOH, S.L. & FEIGENSON, G.W. 2013 Competition between line tension and curvature stabilizes modulated phase patterns on the surface of giant unilamellar vesicles: a simulation study. *Phys. Rev. E* **87**, 022708.
- AMRUŞ, V.E., BUSUIOC, S., WAGNER, A.J., PAILLUSSON, F. & KUSUMAATMAJA, H. 2019 Multicomponent flow on curved surfaces: a vielbein lattice Boltzmann approach. *Phys. Rev. E* **100** (6), 063306.
- BACHINI, E., KRAUSE, V., NITSCHKE, I. & VOIGT, A. 2023a Derivation and simulation of a two-phase fluid deformable surface model. *J. Fluid Mech.* **977**, A41.
- BACHINI, E., KRAUSE, V., NITSCHKE, I. & VOIGT, A. 2023b The interplay of geometry and coarsening in multicomponent lipid vesicles under the influence of hydrodynamics. *Phys. Fluids* **35**, 042102.
- BAR-ZIV, R. & MOSES, E. 1994 Instability and pearling states produced in tubular membranes by competition of curvature and tension. *Phys. Rev. Lett.* **73**, 1392–1395.
- BAR-ZIV, R., MOSES, E. & NELSON, P. 1998 Dynamic excitations in membranes induced by optical tweezers. *Biophys. J.* **75**, 294–320.
- BARRETT, J.W., GARCKE, H. & NÜRNBERG, R. 2017 Finite element approximation for the dynamics of fluidic two-phase biomembranes. *Math. Modelling Numer. Anal.* **51**, 2319–2366.
- BARTHÈS-BIESEL, D. 2016 Motion and deformation of elastic capsules and vesicles in flow. *Ann. Rev. Fluid Mech.* **48**, 25–52.
- BAUMGART, T., HESS, S. & WEBB, W. 2003 Imaging coexisting fluid domains in biomembrane models coupling curvature and line tension. *Nature* **425**, 821–824.
- BOEDDEC, G., JAEGER, M. & LEONETTI, M. 2014 Pearling instability of a cylindrical vesicle. *J. Fluid Mech.* **743**, 262–279.
- CAMLEY, B.A. & BROWN, F.L.H. 2014 Fluctuating hydrodynamics of multicomponent membranes with embedded proteins. *J. Chem. Phys.* **141**, 075103.
- CLAESSENS, M.M.A.E., VAN OORT, B.F., LEERMAKERS, F.A.M., HOEKSTRA, F.A. & STUART, M.A.C. 2007 Bending rigidity of mixed phospholipid bilayers and the equilibrium radius of corresponding vesicles. *Phys. Rev. E* **76**, 011903.
- DESCHAMPS, J., KANTSLE, V., SEGRE, E. & STEINBERG, V. 2009 Dynamics of a vesicle in general flow. *Proc. Natl Acad. Sci.* **106** (28), 11444–11447.
- ELSON, E.L., FRIED, E., DOLBOW, J.E. & GENIN, G.M. 2010 Phase separation in biological membranes: integration of theory and experiment. *Annu. Rev. Biophys.* **39**, 207–226.
- FAIZI, H.A., DIMOVA, R. & VLAHOVSKA, P.M. 2022 A vesicle microrheometer for high-throughput viscosity measurements of lipid and polymer membranes. *Biophys. J.* **121**, 910–918.
- GERA, P. 2017 Hydrodynamics of multicomponent vesicles. PhD thesis, State University of New York, New York, NY.
- GERA, P. & SALAC, D. 2017 Three-dimensional multicomponent vesicles: dynamics and influence of material properties. *Soft Matt.* **14**, 7690–7705.
- GERA, P., SALAC, D. & SPAGNOLIE, S.E. 2022 Swinging and tumbling of multicomponent vesicles in flow. *J. Fluid Mech.* **935**, A39.

Stability of cylindrical, multicomponent vesicles

- GOLDSTEIN, R.E., NELSON, P., POWERS, T.R. & SEIFERT, U. 1996 Front propagation in the pearling instability of tubular vesicles. *J. Phys. II France* **6**, 767–796.
- GRANEK, R. & OLAMI, Z. 1995 Dynamics of Rayleigh-like instability induced by laser tweezers in tubular vesicles of self-assembled membranes. *J. Phys. II* **5** (9), 1349–1370.
- GURIN, K.L., LEBEDEV, V.V. & MURATOV, A.R. 1996 Dynamic instability of a membrane tube. *J. Exp. Theor. Phys. C* **83**, 321–326.
- HAPPEL, J. & BRENNER, H. 1973 *Low Reynolds Number Hydrodynamics*. Noordhoff International Publishing.
- HELFRICH, W. 1973 Elastic properties of lipid bilayers: theory and possible experiments. *Z. Naturforsch. C* **0**, 693–703.
- KANTSLEER, V., SEGRE, E. & STEINBERG, V. 2008 Critical dynamics of vesicle stretching transition in elongational flow. *Phys. Rev. Lett.* **101**, 048101.
- LIPOWSKY, R. & SEIFERT, U. 1995 Morphology of vesicles. In *Handbook of Biological Physics, vol. 1: Structure and Dynamics of Membranes from Cells to Vesicles* (ed. R. Lipowsky & E. Sackman), pp. 403–463. North-Holland.
- LITSCHER, T. & SCHWILLE, P. 2021 Protein reconstitution inside giant unilamellar vesicles. *Ann. Rev. Biophys.* **50** (1), 525–548.
- LUO, Y. & MAIBAUM, L. 2020 Modulated and spiral surface patterns on deformable lipid vesicles. *J. Chem. Phys.* **153**, 144901.
- NAPOLI, G. & VERGORI, L. 2010 Equilibrium of nematic vesicles. *J. Phys. A: Math. Theor.* **43**, 445207.
- NARSIMHAN, V. 2014 Flow dynamics of fluid-filled particles with complex interfaces: a study of surfactant-contaminated droplets, red blood cells, and vesicles. PhD Thesis, Stanford University, Stanford, CA.
- NARSIMHAN, V., SPANN, A. & SHAQFEH, E.G. 2015 Pearling, wrinkling, and buckling of vesicles in elongational flows. *J. Fluid Mech.* **777**, 1–26.
- NEGISHI, M., SETO, H., HASE, M. & YOSHIKAWA, K. 2008 How does the mobility of phospholipid molecules at a water/oil interface reflect the viscosity of the surrounding oil? *Langmuir* **24** (16), 8431–8434.
- PÖHNL, M., TROLLMANN, M.F.W. & BÖCKMANN, R.A. 2023 Nonuniversal impact of cholesterol on membranes mobility, curvature sensing and elasticity. *Nat. Commun.* **14**, 8038.
- POWERS, T.R. 2010 Dynamics of filaments and membranes in a viscous fluid. *Rev. Mod. Phys.* **82**, 607–1631.
- PULLARKAT, P.A., DOMMERSNES, P., FERNÁNDEZ, P., JOANNY, J.F. & OTT, A. 2010 Osmotically driven shape transformations in axons. *Phys. Rev. Lett.* **96** (4), 048104.
- RAHIMI, M., DESIMONE, A. & ARROYO, M. 2011 Curved fluid membranes behave laterally as effective viscoelastic media. *Soft Matt.* **9** (46), 11033–11045.
- SAFRAN, S. 2018 *Statistical Thermodynamics of Surfaces, Interfaces, and Membranes*. CRC Press.
- SAHU, A., SAUER, R.A. & MANDADAPU, K.K. 2017 Irreversible thermodynamics of curved lipid membranes. *Phys. Rev. E* **96** (4), 042409.
- SAKUMA, Y., KAWAKATSU, T., TANIGUCHI, T. & IMAI, M. 2020 Viscosity landscape of phase-separated lipid membrane estimated from fluid velocity field. *Biophys. J.* **118** (8), 1576–1587.
- SEIFERT, U. 1997 Configurations of fluid membranes and vesicles. *Adv. Phys.* **46**, 13–137.
- SHIMSHICK, E.J. & MCCONNELL, H.M. 1973 Lateral phase separation in phospholipid membranes. *Biochemistry* **12**, 2351–2360.
- SIMONS, K. & IKONEN, E. 1997 Functional rafts in cell membranes. *Nature* **387**, 569–572.
- SURYO, R., DOSHI, P. & BASARAN, O.A. 2007 Nonlinear dynamics and breakup of compound jets. *Phys. Fluids* **18**, 082107.
- TOMOTIKA, S. 1935 On the instability of a cylindrical thread of a viscous liquid surrounded by another viscous fluid. *Proc. R. Soc. Lond. A* **150**, 332–337.
- VEATCH, S. & KELLER, S.L. 2003 Separation of liquid phases in giant vesicles of ternary mixtures of phospholipids and cholesterol. *Biophys. J.* **85** (5), 3074–3083.
- VLAHOVSKA, P.M. & GRACIA, R.S. 2007 Dynamics of a viscous vesicle in linear flows. *Phys. Rev. E* **75** (1), 016313.
- WOLFF, J., MARQUES, C.M. & THALMANN, F. 2011 Thermodynamic approach to phase coexistence in ternary phospholipid-cholesterol mixtures. *Phys. Rev. Lett.* **106** (12), 128104.
- YANAGISAWA, M., IMAI, M. & TANIGUCHI, T. 2010 Periodic modulation of tubular vesicles induced by phase separation. *Phys. Rev. E* **82**, 051928.
- YOON, S., JEONG, D., LEE, C., KIM, H., KIM, S., LEE, H.G. & KIM, J. 2020 Fourier-spectral method for the phase-field equations. *Mathematics* **8** (8), 1385.
- YU, Q. & KOŠMRLJ, A. 2023 Pattern formation of phase-separated lipid domains in bilayer membranes. Preprint, [arXiv:2309.05160](https://arxiv.org/abs/2309.05160).